Document Number**:** H2020-ICT-52/RISE-6G/D3.2

Project Name:
Reconfigurable **I**ntelligent **S**ustainable **E**nvironments for **6G** Wireless Networks (RISE-6G)

Deliverable 3.2

RIS designs, and first prototypes characterization

Date of delivery:	29/07/2022	Version:	1.0
Start date of Project:	01/01/2021	Duration:	36 months

Deliverable D3.2
RIS designs, and first prototypes characterization

Project Number:	H2020-ICT-52 / 101017011
Project Name:	**R**econfigurable **I**ntelligent **S**ustainable **E**nvironments for **6G** Wireless Networks

Document Number:	H2020-ICT-52/RISE-6G/D3.2
Document Title:	RIS designs, and first prototypes characterization
Editor(s):	J. B. Gros (GNW)
Authors:	CEA: S.Garbieh, A. Clemente, R. D'Errico, GNW : J. B. Gros AAU : O. Franek NKUA : G. Alexandropoulos, I. Vinieratou ORA : P. Ratajczak CHAL : Z. S. He
Dissemination Level:	PU
Contractual Date of Delivery:	31/06/2022
Security:	Public
Status:	FINAL
Version:	1.0
File Name:	RISE-6G_WP3_D3.2_Final.docx

Abstract

This document describe the first RIS designs and prootypes developed in the framework of RISE-6G. Different Transmitting, Reflecting, Dual or Hybrid designs are presented based on different technologies (PiN diodes, MEMS, Varactors). The designs are being developed to cover different bands of interest in sub-6GHz, mmW and THz bands.

Keywords

RIS, Unit Cell, Antenna

Contents

List of Figures

List of Tables

1 Introduction

The general objective of RISE-6G WP3 is to model, design, and characterize the RIS components as a part of the overall system for enhanced connectivity, localisation and sensing, as well as sustainability. The RIS prototypes developed in this WP will also be integrated in the final project demonstrations and PoCs.

Here we tackle the main technology challenges related to the design and prototyping in a large frequency range from sub 6 GHz up to D-band of RIS based on different core technology from simple pin diode to more complex MEMS or varactor.

The general objective of this deliverable is to report the methodology to:

- **Design, prototype and characterize the RISs and control logic for the PoC**

1.1 Definitions

Reconfigurable intelligent surfaces (RISs) are surfaces composed of a discrete set of antenna elements following the generalised Snell's law, and can be seen as **reflective or transmissive electromagnetic surfaces** as a function of the selected operation mode. Specifically, **a reflective surface (R-RIS)** operates as an electromagnetic mirror, where an incident electromagnetic wave is reflected towards the desired direction, typically anomalous in the sense that this direction is non-specular, with specific radiation and polarisation characteristics. On the other hand, a **transmissive RIS (T-RIS)** operates as a lens or a frequency selective surface, where the incident field is manipulated (by filtering, polarisation, beam splitting, etc.) and/or phase shifted, and re-radiated so as to control the refraction of plane impinging waves. Although RISs have great potential to implement advanced electromagnetic wave manipulations, only simple functionalities, such as electronic beam-steering and multi-beam scattering, have been demonstrated in the literature. Recently, some investigators have touched upon the possibility of deflecting the beam to achieve **simultaneous reflective-transmission RIS (RT-RIS)** [WDB18].

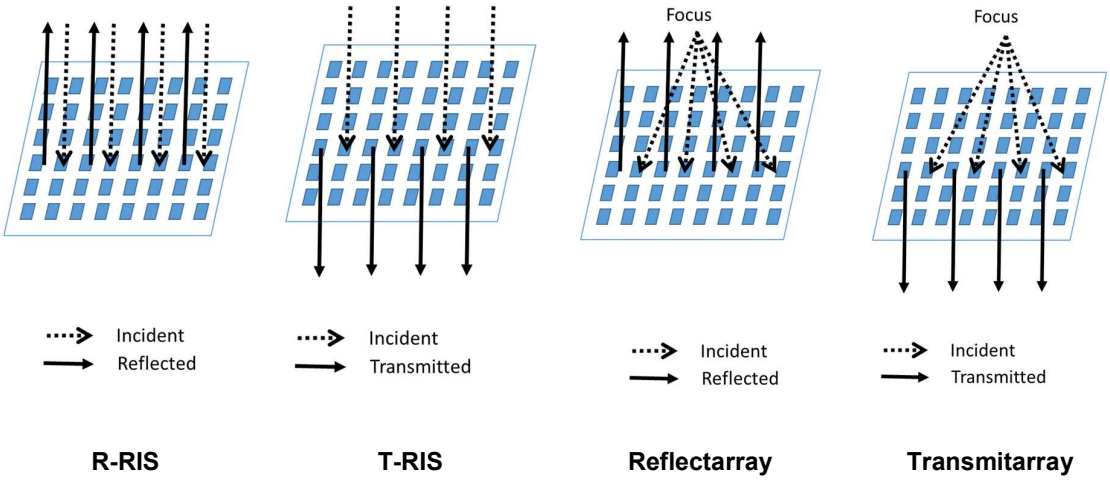

Figure 1-1 – RIS taxonomy

Several different antenna technologies (e.g., [GTB16], [SN17]) can be considered as RIS hardware technologies, including **reflectarrays** [HPC14], **transmitarrays** (e.g., [DCD20], [DCS20], [RVC19]), as well as smart, programmable or software-defined metasurfaces (e.g., [BMM20], [YCY16], [TBM14], [ZZZ10], and [DGL20]).

When the elements have both size and spacing **lower than 1/10th** of the communication operation wavelength, RISs are also **defined as metasurfaces** [GTB16]. Metasurfaces are artificial materials able to manipulate electromagnetic waves, in a way that cannot be performed in homogeneous materials. Simple functionalities enabled by metasurfaces include anomalous reflections or transmissions. Achieving **perfect** anomalous reflection and refraction is possible if metasurfaces are bianisotropic with weak spatial dispersion [AAT16]. Spatially dispersive metasurfaces are realized as artificial sheets, which are typically composed of metallic patches or dielectric engravings in planar or multi-layer configurations within subwavelength thickness. The interaction with electric and/or magnetic fields, is typically provided by resonant effects controlled by the geometry of the unit cells and their distribution, enabling antenna performance enhancement (beamshaping), flat lens, artificial magnetic conductors, cloaking, absorbers and scattering reduction. In particular, the introduction of programmable metasurfaces could realize intelligent environments---giving birth to the novel concept of Environment as a Service (EN-VaaS)---where such metamaterials act as smart reflectors to enhance coverage and open new technical and business opportunities for beyond-5G (and 6G) networks.

Compared to classical phased arrays, which require phase-shifters and power amplifiers, RISs are generally passive radiative architectures integrating switches, RF-MEMS, p-i-n diodes, varactors, and/or liquid crystals, to control electronically the local surface phase-shift and/or impedance characteristics. So according to the technology of the unit cell (UC) we can distinguish **between active RIS**, where the reflected signal is amplified by an active element in UC, and **passive RIS,** where the UC is realized with low loss reactive components that are used to implement a prescribed phase shift, either continuous or quantized, resulting in low-energy device.

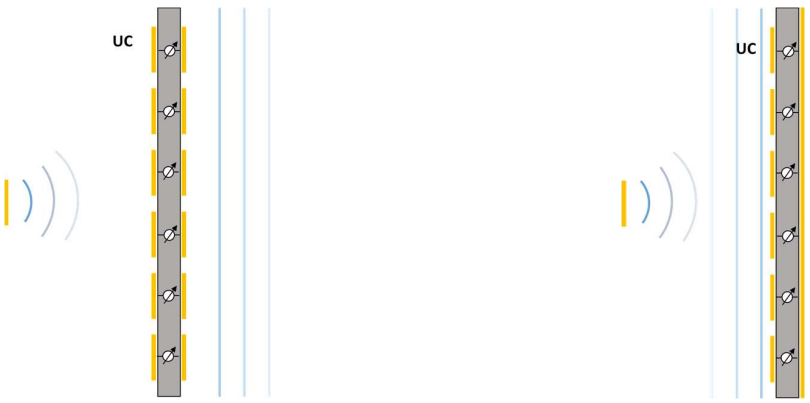

Figure 1-2 – Typical RIS passive architecture: T-RIS/Transmitarray (a), R-RIS/Reflectarray (b)

Finally, as for relays we can also distinguish different operating modes: **Regenerative RIS** that decode, regenerate and retransmit a copy of the original signal; **Non-Regenerative RIS** that act as analog repeaters by retransmitting the signal they receive (in some cases amplified through beamfoming techniques or active elements). A receiving RIS (RX-RIS) enables measurement collection at its site, through a single or few Receive (RX) Radio-Frequency (RF) chains

attached to all or a subset of the its unit elements [AV20]. A hybrid surface (H-RIS) combines two of the above-mentioned modes, being able to reflect the impinging signal and simultaneously sense/measure a part of it [ASA21], [ZSA21].

In this context, RISE-6G investigates RIS over a wide span: suggested prototypes are mainly with UCs separation of half-wavelength. However, different studies include metasurfaces, e.g., dipole-based metasurfaces that are considered to address the theoretical performance evaluation of RIS assisted wireless systems when the RIS is based on metasurface structures, i.e., including mutual coupling between subwavelength UCs. Prototypes of T-RIS, R-RIS and simultaneous RT-RIS are addressed theoretically and experimentally. From the technology point of view mainly passive RIS based on p-i-n diodes, RF-MEMS and varactors are addressed below 40 GHz. Above these frequencies, active UCs are considered too.

2 RIS design and prototyping

2.1 Introduction

As presented before in the SoTA, RISs are fabricated similarly to known antenna concepts, which need to be opportunely redesigned to take into account the multi-function, EE, scalability, and flexibility paradigms required in B5G and envisioned for future 6G networks. In SoTA, several fixed-beam architectures based on reflectarrays, transmitarrays, or metasurfaces have been demonstrated up to sub-THz [GTB16], but in the case of electronically-tunable RISs, excluding the pioneer demonstrations of the RISE-6G's partners CEA, GNW, and CHAL d the complex phased arrays based on monolithic microwave integrated circuits [SGV19], only few prototypes have been demonstrated up to the Ka-band (26-40 GHz).

Recently it has been suggested to equip RISs with receiving antennas in order to extract information about the wireless channel from the impinging signal at the RIS [AV21], [TAA21]. This way, the overhead costly procedure of estimating the cascaded channel is avoided. In [LPP19], it is proposed to use the concept of Hypersurfaces with a control network that iterates over the active element states until the power sensed is maximized. The channel estimation is obtained by comparing the element states with a lookup table that contains the states to achieve full absorption for specific impinging waves. In [MBJ19] the smart meta-surface integrates additional sensors and controls the meta-surface with a sensing feedback system. The authors of [ASA21] introduce the concept of a Hybrid Reconfigurable Intelligent Surface (HRIS) that reflects and simultaneously senses a portion of the impinging waves. In [AAS21], a full-wave proof-of-concept and hardware design for an HRIS (a small portion of the incident wave is coupled to an array of sensing waveguides and the rest is reflected) is presented and the sensing capability is demonstrated with an AoA estimation example. Finally, in [ZSA21], for a multi-user uplink system empowered with HRIS, the individual channels identification problem is solved, and the results show notably reduced overhead.

In this chapter we present the main concepts and designs developed in the RISE-6G. The final prototyping will be fixed based on the demonstrator needs in WP7.

2.2 Review of RISE-6G RIS unit cells and full RIS designs and characterization

In this section we present our RIS development methodology and review the design progress of the various RIS developed by the RISE-6G partners. Some designs are at the stage of numerical design and characterisation of the basic building block of RIS, namely unit cells, while others are full RIS that have already been fabricated and tested. These full RIS are either one-off laboratory prototypes or ready-to-use product RIS, which means that for the latter their design is almost ready for industry and they can be manufactured quickly in a required number of samples with a plug and play interface.

The review of designs is organized according to the technology platform used to make RIS re-configurable. We start with PIN diode-based RIS, then successively MEMS-based RIS, RF switches-based RIS, varactors-based RIS and finally integrated circuits-based RIS.

2.2.1 Binary Reflective RIS based on PIN diode design in Ka band and sub-6GHZ.

We describe in the following the procedure used to design the fisrt Greenerwave RIS working at mmW frequencies. This procedure is quite generic at Greenerwave but also for the other RISE-6G partners.

A. Unit cell design

The single unit cell (or pixel) of the designed metasurface (1) is represented by a conducting square patch (made of copper) placed on a low loss grounded dielectric substrate Meteorwave 8000 (ε = 3.3 @ 10 GHz, tan(δ) = 0.0016 @ 10 GHz) [V. L. L. P. M.]. At the resonance frequency of the patch the incident wave strongly interacts with the unit cell leading to enhanced power dissipation and significant phase advance of the reflected wave. The unit cell is designed to provide the patch resonance f_0 to be approximately around 27.5 GHz.

In order to provide the proper operation of the binary reflect array, two conditions should be fulfilled: the amplitude of the reflected wave should be maximum and the reflection phase should be able to switch in 2 states with a π-phase difference. There are many ways to change the phase of the reflected wave and most of them are based on changing the electrical length of the resonator. The simplest way to do it is to shunt the patch resonator onto the ground using an active element i.e. PIN diode. Nevertheless, this leads first to a strong dissipation growth due to increased current through the PIN diode. Moreover, this system becomes quite sensitive to the fabrication intolerances of the diodes. Due to this reason here we use a different method to control reflection phase. In order to provide a π-phase shift, the design of the pixel is complemented with a parasitic resonator (P_H and P_V on Fig.1a for both corresponding horizontal and vertical polarizations of the E-vector of incident wave). The resonance frequency of the parasitic resonator lies close to the resonance of the patch. That leads to appearance of strong coupling between two resonators and corresponding anti-crossing behaviour when coupled resonances repulse and the mutual resonance shifting occurs. While changing the electrical length of the parasitic resonator we change its resonance frequency and can tune the mutual coupling between resonant modes of the parasitic resonator and the patch. This in turn allows to change the resonance frequency of the patch and the phase of the reflected wave at a given frequency. This method was first suggested and verified in [N. Kaina, M. Dupré, M. Fink, and G. Lerosey, “Hybridized resonances to design tunable binary phase metasurface unit cells,” Opt. Express, vol. 22, pp. 18881–18888, Aug 2014]. In order to provide control of the electrical length of the parasitic resonator, it is split into two parts connected with a PIN diode (MACOM-000907). To make the unit cell more compact the parasitic resonator is partially placed inside the preliminary carved patch resonator. The diode state is switched via applied voltage or current, controlled through the biasing network. The network is isolated from the RF- part of the unit cell through the lumped inductive elements (chokes). To increase the structure symmetry, one of the chokes of the parasitic resonator which is the closest to the patch is placed in the middle of the resonator and is connected to the patch. The patch is then connected with the other pole of the control network through the common patch choke, which is placed on the right side of the patch (see Figure 2-1.a). Electrical connection to the biasing network between top and bottom layers is provided through the vias. All the control electronics is placed on the back side of the multilayer PCB. When we apply a 5V biasing voltage, the state of the PIN diode is changed from isolating (we call it *OFF-state*) to conducting (*ON-state*). The electrical length of the parasitic resonator changes correspondingly providing shifting of its own resonance frequency and consequently of the resonance frequency of the main patch. Figure 2-1..b) shows simulated reflection coefficient from the infinite periodic structure composed of the described pixels. The simulation was performed with the time domain solver of the CST Studio Suite software. The unit-cell is simu-

lated in the rectangular waveguide (WR-34) as illustrated by Figure 2-1.a). A single-mode rectangular waveguide port is set two wavelength (at 28.5 GHz) away from the top of the unit cell. However, the simulation is performed in a wide frequency range and at the lowest frequency the distance to the port is approximately one wavelength. The port is de- embedded having the reference plane at the top of the unit cell in order to subtract the propagation phase. In the OFF-state the resonance of the patch (27.5 GHz, in Figure 2-1.b)) lies to the left of the resonance of the parasitic resonator (30 GHz at Figure 2-1..b)). In the ON-state the electrical length of the parasitic resonator increases and the parasitic resonance is shifted to the lower frequency (22.5 GHz). The coupled patch resonance is correspondingly pushed to the higher frequency (29.5 GHz). The operating frequency range of the unit cells is defined from the acceptable level of the reflection coefficient amplitude and difference of the reflection coefficient phases between ON- and OFF-states. To operate, a RIS is required to modify the phase of the reflected wave in comparison to the incident wave and not to dissipate all the incident power. The maximum phase difference possible is 180 degrees, but any value close to it is enough. For the designed pixel shown in Figure 2-1. a), the operating frequency range lies in the frequency band from 27.5 GHZ to 29.5 GHz. In this range, marked with the two vertical dashed lines in Figure 2-1.b), independently of the pixel's state, the phase difference is always larger than 160°. Meanwhile, the reflection amplitude level never goes under the -5 dB level, meaning that more than 20% of power is reflected. Although these characteristics are not perfect and they can be further improved.

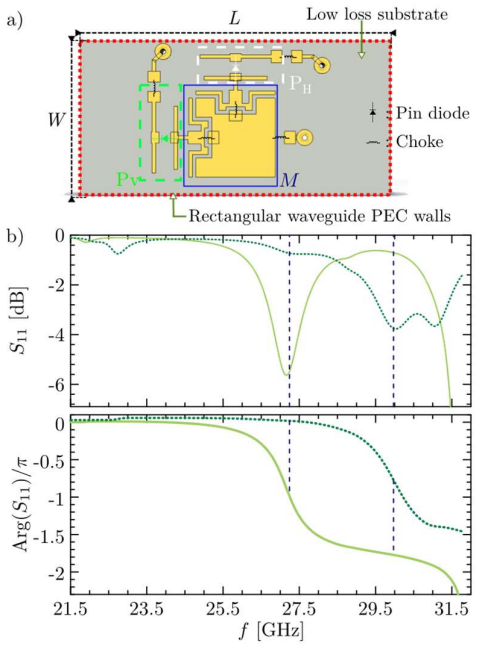

Figure 2-1 a) Unit cell of the designed RIS. M - main patch, PH and PV are horizontal and vertical parasitic resonances respectively. When studied experimentally the pixel is placed inside the WR-34 hollow waveguide. b) Simulated reflection from the metasurface unit cell. Solid line represents OFF-state and doted line represents ON-state of the pixel. Vertical dashed lines show the operating frequency range of the pixel.

B. Unit cell measurements

To experimentally verify the properties of the designed pixel a set of pixels with slightly variable dimensions of resonators was fabricated. The WR-34 rectangular waveguide was used to characterize reflection properties of the single pixel. The pixel size was adjusted to fit the waveguide aperture (W×L= 0.34×0.17 inches). In order to avoid leakage of the field through the pixel substrate and provide isolation of the field inside the waveguide, a periodic via structure was formed at the edge of the pixel acting as an artificial electric wall. The bias network vias are connected with the pins on the back side of the pixel for the power supply connection. In order to place electronics on the back side of pixel there is a FR-4 substrate placed under the radiofrequency grounding layer (RF-ground). That is, single pixel consists of 2 layers of substrate separated by the ground layer. The pixel is tightly attached to the flange of the WR-34 waveguide in order to provide proper electrical connection with the waveguide. The waveguide (which is also the waveguide to coaxial adapter) is connected to a Rohde & Schwarz ZVA-40 vector network analyzer . In order to provide reflection state control, the electrical pins of the diodes, placed on the back side of the pixel, were connected to the constant voltage power source. The OFF-state of the diode was provided by the 0-voltage applied to the anode of the diode. The ON-state was provided by the -5V voltage applied to the cathode of the diode. The measured reflection properties of the single pixel inside a rectangular waveguide is shown on Figure 2-2. We see that we can indeed control the phase difference of the reflection coefficient by changing the position of the main patch resonance coupled with the resonance of parasitic resonator. In the 2 GHz frequency range between 27.5 GHz and 29.5 GHz the phase difference between ON and OFF states is between 144° and 180°. The reflection amplitude in this range doesn't drop below -6 dB and average value in the frequency range bet wen 2 states is equal to -3 dB reaching -1 dB for some of the frequencies. It is worth noting that during the operation of the RIS, the average number of pixels in ON and OFF state are approximately equal. The difference between the simulated and the experimental results can be explained by the following reasons. First there is the way we simulate the properties of the lumped components (PIN diodes, chokes). The equivalent RLC-model is used to describe the diodes and chokes properties and the parameters of the model may differ from the properties of real components. Secondly, in the simulation model, we don't consider the effect of the FR4 layer placed behind the RF-ground.

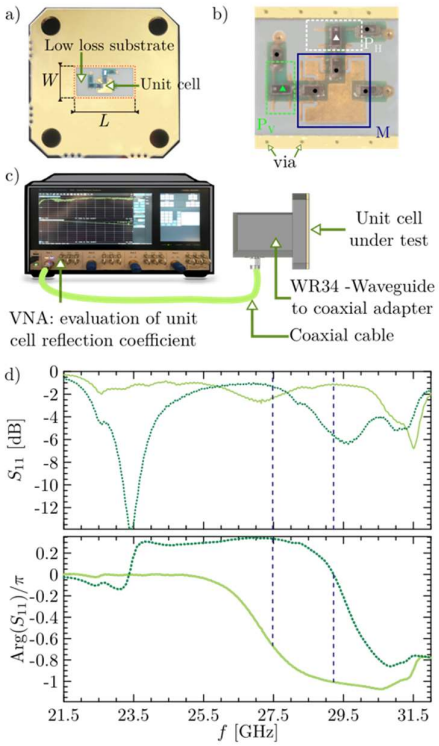

Figure 2-2 a) Pixel fabricated for the waveguide characterization. The big copper area around is intended to form electrical contact with the waveguide flange. b) Magnified photo of the fabricated pixel. The vias around provide isolation of the field inside waveguide. M, PH and PV are main patch, horizontal and vertical parasitic resonator respectively. Dots and triangles tag respectively chokes and pin diodes. c) The setup of the experiment. d) Measured reflection from the single pixel inside the rectangular WR-34 waveguide. Solid line represents OFF-state and doted line represents ON-state of the pixel. Vertical dashed lines correspond to frequency where actual π-phase shift occurred showing the operating frequency range of the pixel

C. Reconfigurable intelligent surface fabrication

After the validation of the properties of 30 different pixels inside the waveguide the geometry which provides lower dissipation and better phase shift is selected. The selected pixel is used for fabricating the metasurface acting as a a reconfigurable intelligent surface (RIS). We fabricate a 10 × 10 cm² RIS – approximately 10×10λ (λ is a wavelengths at 30 GHz) – made up of 400 unit cells periodically placed every λ/2 = 0.5 cm on a rectangular lattice of 20 × 20 pixel as shown by Figure 2-3. a). Each unit cells having to control independently both components of the reflected EM field, an overall of 400 diodes to control vertical polarisation and 400 diodes to control horizontal polarization are used. More technically speaking, our RIS consists in a 6 layer PCB. The first layer is made from a low loss substrate, namely the METEORWAVE 8000 from AGC, and supports the 400 unit cells (see front view in Figure 2-3.a)). The 5 remaining layers are made from FR4 substrate. The last layer shown in Figure 2-3.b), notably supports the electronic components that allow us to control the states of the diodes of the pixels on the first layer. This control is operated by a 10 × 10 matrix of shift registers, each of them managing the states of 8 PIN diodes associated to the horizontal and vertical polarization states of 4 pixels. In order to provide control of each pixel of the RIS, a FPGA control board has been designed and programmed (see Figure 2-3. c)). This control board has 4 ports to connect 4 independent RIS. The control board is connected to the desktop through LAN or USB interface and is controlled with a Python or MATLAB code. The developed software allows to independently change the

state of each diode on the RIS providing the required reflection properties across the whole RIS. PIN diodes are thus connected to the control board through the network of shift registers. We should point out that the assembly composed by the RIS and the FPGA control board shown in Figure 2-3is a very low power consuming RIS. Indeed, it consumes in average no more than 4 Watts, with a potential peak power of 8 Watts if all diodes are in ON-state. This power consumption can even be more reduced by tuning of the bias voltage applied to diode. In practice, in more recent version of our RIS, we have been able to reduce this power consumption by a factor of two. A last interesting propriety of our RIS is its switching state rate. While remotely controlling from a desktop, the latter lies in a kHz range. If the pattern of the PIN diode states is stored locally on the board, update rate reaches nearly 100 kHz. Current maximum speed is function of the shift register chain organization.

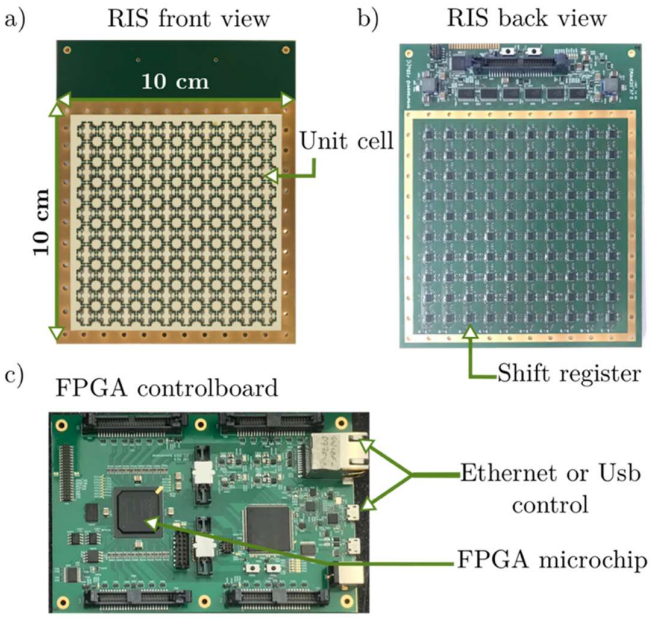

Figure 2-3 a) Front and b) back side of the fabricated 10 × 10 cm² RIS. c) RIS control board with different interfaces

D. RIS properties improvement

As the RIS losses are directly correlated to the pixel dissipation, it appeared necessary to develop pixels with dissipations below 3 dB. By going back to the experimental cratering of the pixel, it appears that the main source of dissipation comes from the high quality factor of the main patch. By playing on this quality factor, we have a lever to reduce the dissipation of the pixels. A new pixel has been therefore designed, based on a slightly different geometry but above all a thicker substrate in order to reduce the dissipation due to the resonance of the main patch.

As the change in substrate thickness requires a slightly larger main resonator, the pixel no longer fits into a WR34 waveguide, so it was characterised in free space using a method based on mini-metasurfaces Figure 2-4. In contrast to the waveguide approach, in which the waves emitted in the waveguide remain confined by propagating via the propagative modes, the free space method is by definition performed in open space. We have chosen to use a bistatic characterisation approach inspired by existing work [DRR00]. Using the same iterative approach as

for the first version, a pixel with an average dissipation of -2 dB was obtained (Figure 2-5). This pixel have been integrated into two new kind of RIS (Figure 2-6).

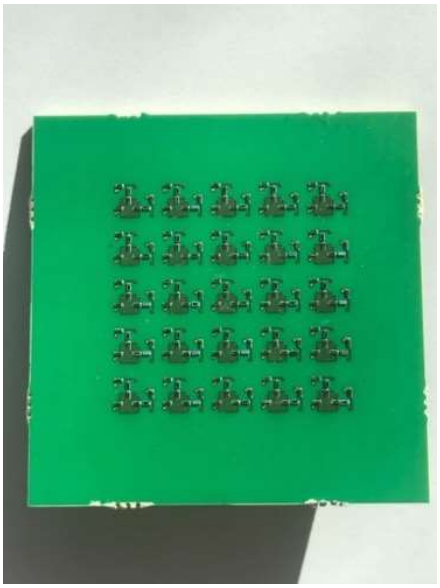

Figure 2-4 Example of a sample operating at 28 GHz fabricated for free space testing.

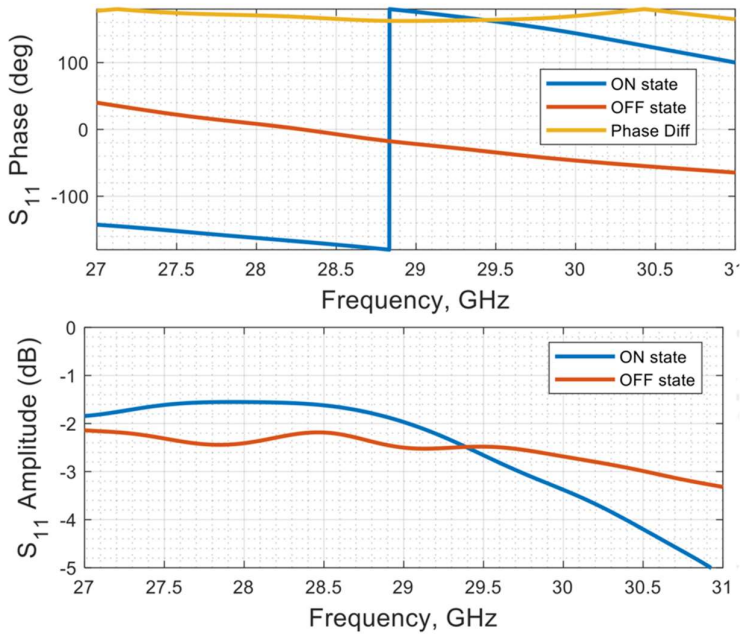

Figure 2-5 Free space characterization of V2 pixel

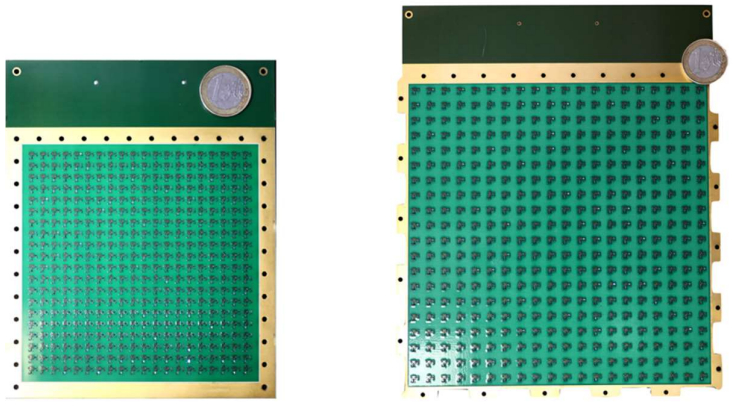

Figure 2-6 10 cm x 10 cm and 15 cm x 15 cm RIS with λ/2 spacing and 3 x λ/2 spacing (ie 400 x2 polarization elements)

E. RIS packaged for application

When the design of RIS have been validated, we can begin to assemble them with respected to the applications need. For instance the RIS of Figure 2-6 have been integrated in Greenerwave mmW access point extenders Figure 2-7. The total RIS size inside the access point extender is 200 mm x 200 mm. The RIS is controlled by MATLAB or Python software and is capable to operate in the Far-to-Far field and Near-to-Far field regime. The RIS by reflecting the electromagnetic signal is capable to perform single or several beams with controllable beam direction, frequency, polarization, and beamwidth. The beam switching rate reaches hundreds of milliseconds.

Since the RIS is inherently passive structure, it has a very low power consumption (few Watts in the idle mode and 18 W average in operational mode). The current access point extender is based on RIS having a low RF dissipation level below 2.5 dB in reflection and new generation of RIS with a even lower dissipation (about 1.5 dB) is under development.

The RIS and the mmW access point extender based on this RIS have an industry ready design and can be rapidly fabricated in a required number of samples.

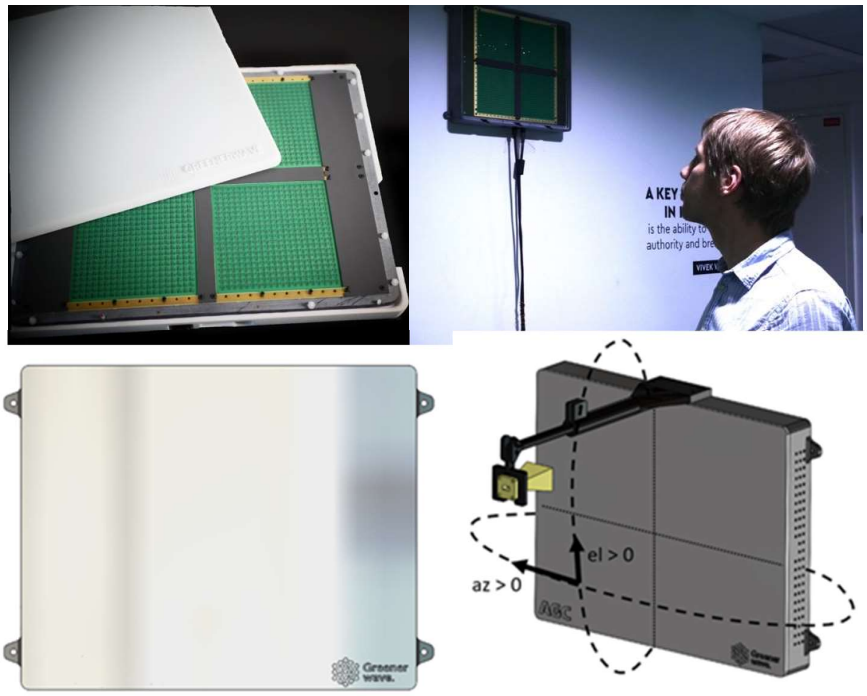

Figure 2-7 Top figures: Bottom figures: Packaged RIS in mmW access point extender. Greenerwave's access point extender view: front and perspective

The specifications of the current mmW access point extender base on RIS are provided in Table 2-1

Table 2-1: Greenerwave's RIS specification

Supply Voltage	5VDC/200mA (USB), 12V/4.5-5A Barrel Jack 5.5mm/2.5mm
Operating Temperature(ambient)	5 ~ 40 °C
Active RIS surface	200 mm * 200 mm
Outline case dimension	350 mm * 260 mm * 40 mm
Weight	1.6 kg
Type connectors	micro USB & ethernet
Power Consumption	ave. 20W, max 40W, min 2W

Freq. range of operation	27.0-31.0GHz
Instantaneous bandwidth	500 MHz
Polarization	dual, H-pol and V-pol
Half power beam width	3-5 degree
Scan Range (Azimuth, Elevation)	+/- 60 deg.
RF Power Handling	max 50W

Software OS	Windows10 and Ubuntu(Linux)
Program language	Python 3.8.x

The Packaged RIS can be easily used and have been tested both in anechoic chamber and in more realistic environment with software define radio setup Figure 2-8. Together with up-, down-converters and local oscillators, a SDR can be used in the following scenarios for different proof-of-concept experimental demonstrations at mmW:

- Non-line-of-sight (NLO) RIS-assisted communication (see a schematic below)
- User equipment tracking with RIS
- Point-to-point communication between two antennas: an electronically scanned array as Rx or Tx and a fixed antenna as Tx or Rx
- Receiver or transmitter tracking with an electronically scanned array

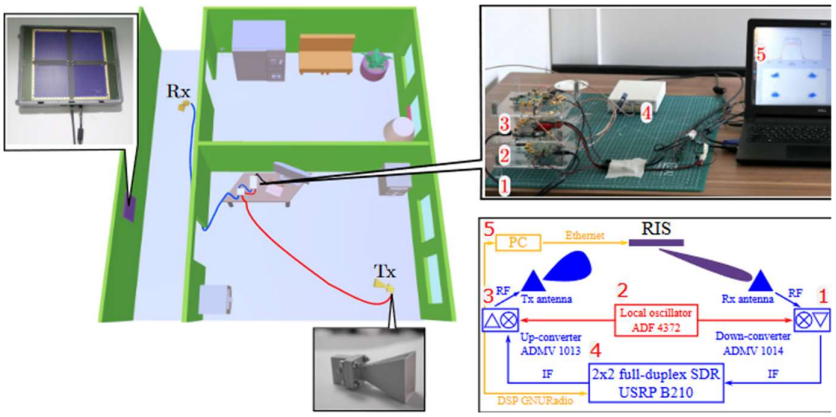

Figure 2-8 Left: A 3D illustration of the experimental setup used to demonstrate RIS-aided indoor wireless communication in a NLOS situation. Right: A photography (top panel) and a schematic (bottom panel) of the communication module represented by a down-converter 1, a local oscillator 2, an up-converter 3, a SDR 4, a PC 5.

D. 3.6-GHz-band 5G reconfigurable intelligent surface (RIS) design

Using the same approach that the one describe above, Greenerwave are also designing new RIS for sub-6GHz application. The designing part is finished and the experimental characterization is ongoing.

The proposed RIS geometry is shown in Figure 2-9(a) with a 5x5 mini-metasurface configuration for comparison with experimental measurements. The reflection coefficient in the two different states is shown in Figure 2-9. b). As it can be seen, the reflector maintains a low dissipation (|S11| > - 2.4 dB) all over the 3.6 GHz band (3.4 - 3.8 GHz). In the desired 3.6 GHz frequency range the phase difference between ON and OFF states is between 163° and 206°.

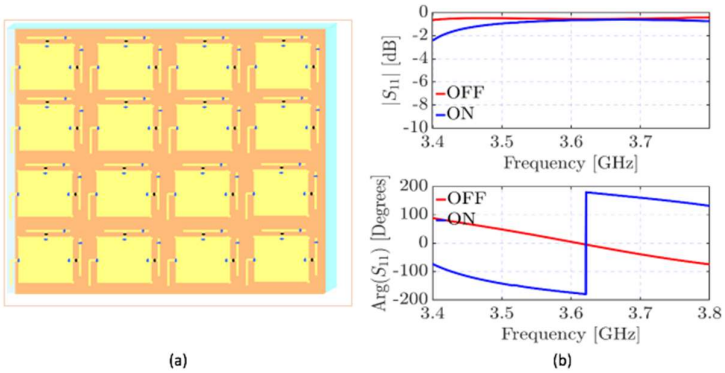

Figure 2-9 : (a) Proposed metasurface geometry. (b) Simulated amplitude and phase of the reflection coefficient of the RIS pixel in the operating range of frequency. Blue line represents OFF-state and red line represents ON-state of the pixel.

Ready to use sub-6GHz RIS will be available for test end of September 2022.

2.2.2 Transmitive-Reflective unit cell RIS design in the Ka band based on PIN diode

The exploded view of the proposed linearly-polarized unit-cell is shown in Figure 2-10. It is composed of six metal layers printed on three (four in the case where an additional layer will be used to implement the bias network of a large array) Isola Astra MT77 substrates (ε_r = 3, tanδ = 0.0017) and bonded with two (or three) Astra MT77 pre-preg bonding films (ε_r = 2.95, tanδ = 0.0019). The bottom and upper metal layers are labelled M1 and M6, respectively. The radiating elements consist of center-fed O-slot rectangular patch antennas working in receive (*Rx*) and transmitting (*Tx*) modes, respectively. These two patch antennas (Figure 2-10 2(b),(g)) are connected by a metalized via hole located at their center and are separated by a ground plane. Two p-i-n diodes MA4AGP907 are flip-chipped on each patch antenna to tune the transmission phase; they are controlled by two bias lines printed on the opposite side of each patch substrate (Figure 2-10 (c),(f)). The bias networks include microstrip radial stubs (M2) and capacitors (M5) to isolate the RF signals in transmission and receive sides, respectively. The DC connection to ground (M4) is realized with a short circuit stub (M3) (Figure 2-10(e)).
The p-i-n diodes are modeled by lumped-elements equivalent circuits validated by specific measurements up to 40 GHz; this model, previously extracted from on-PCB measurements, consists of a series circuit (R_{ON} = 4.2 Ω, L_{ON} = 0.05 nH) and a shunt circuit (R_{OFF} = 300 kΩ, C_{OFF} = 42 fF), in the forward (I_{bias} = 10 mA) and reverse (V_{bias} = 1.2 V) state, respectively (see Figure 2-11).
The two p-i-n diodes on each radiating element are biased in opposite states (one p-i-n diode is switched ON while the other one is in OFF state). Switching between these two states leads to opposite surface-current on the receiving metal layer, named Rx-01, and Rx-10 as shown in Figure 2-12(a) and Figure 2-12(b), respectively. Thus, a 0°/180° phase-shift is achieved on the *Rx* patch antenna. Two distributions of surface-current are also observed on the transmission metal layer labelled Tx-01 and Tx-10, as illustrated in Figure 2-12(c) and Figure 2-12 (d), respectively. Moreover, an additional 90° phase-shift is obtained on the *Tx* patch antenna thanks to the delay line printed on the opposite side of its substrate. As a result, four phase states (0°, 90°, 180° and 270°) are obtained in transmission by combining different states of the receive and transmission layers. The phase configurations are summarized in Table 2-2.

Phase-shift state	*Tx* phase state	*Rx* phase state
0°	**Tx-01**	**Rx-10**
90°	**Tx-10**	**Rx-10**
180°	**Tx-01**	**Rx-01**
270°	**Tx-10**	**Rx-01**

Table 2-2: Different combinations of receive and transmission layers corresponding to the four phase states.

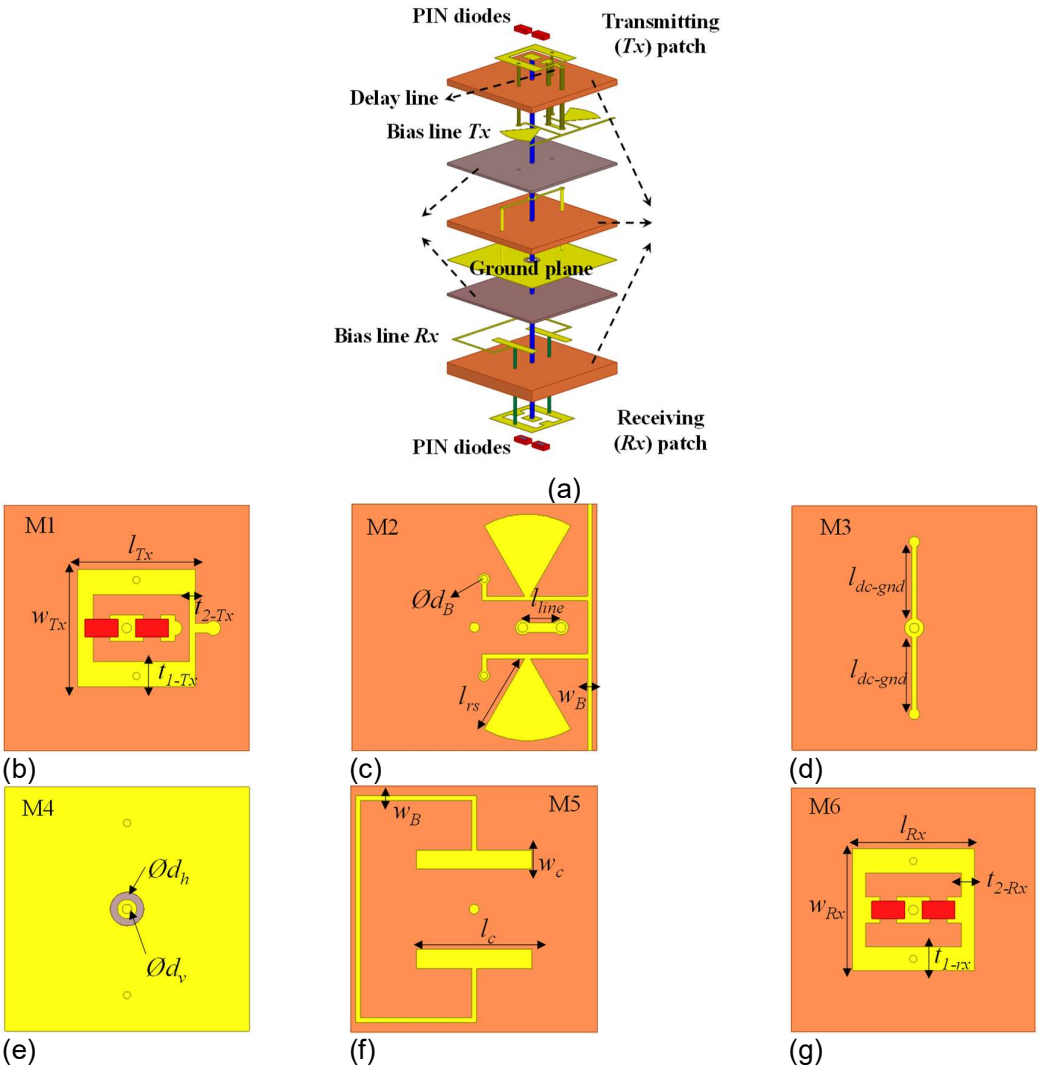

Figure 2-10: Proposed 2-bit linearly-polarized unit-cell: (a) Schematic view, (b) transmitting layer, (c) biasing layer of the transmission side, (d) DC connection to the ground layer, (e) ground plane, (f) biasing layer of the receive side, and (g) receiving layer.

Figure 2-11: Equivalent lumped-elements models of the p-i-n diode in the ON and OFF states.

This 2-bit unit-cell has been simulated for its four phase states using the commercial software Ansys HFSS with periodic boundary conditions on the unit-cell lateral faces and Floquet port excitations on both sides of the element as depicted in Figure 2-12. This method reproduces the characteristics of an infinite array of identical unit-cells in the same states. The full-wave simulations have been performed under normal incidence. In the simulation, the diodes are considered as lumped elements, thus their states are equivalent to a parallel circuit of a capacitor and a resistor in the off-state (Figure 2-12) and to a series circuit of an inductor and resistor in the on-state (Figure 2-12.

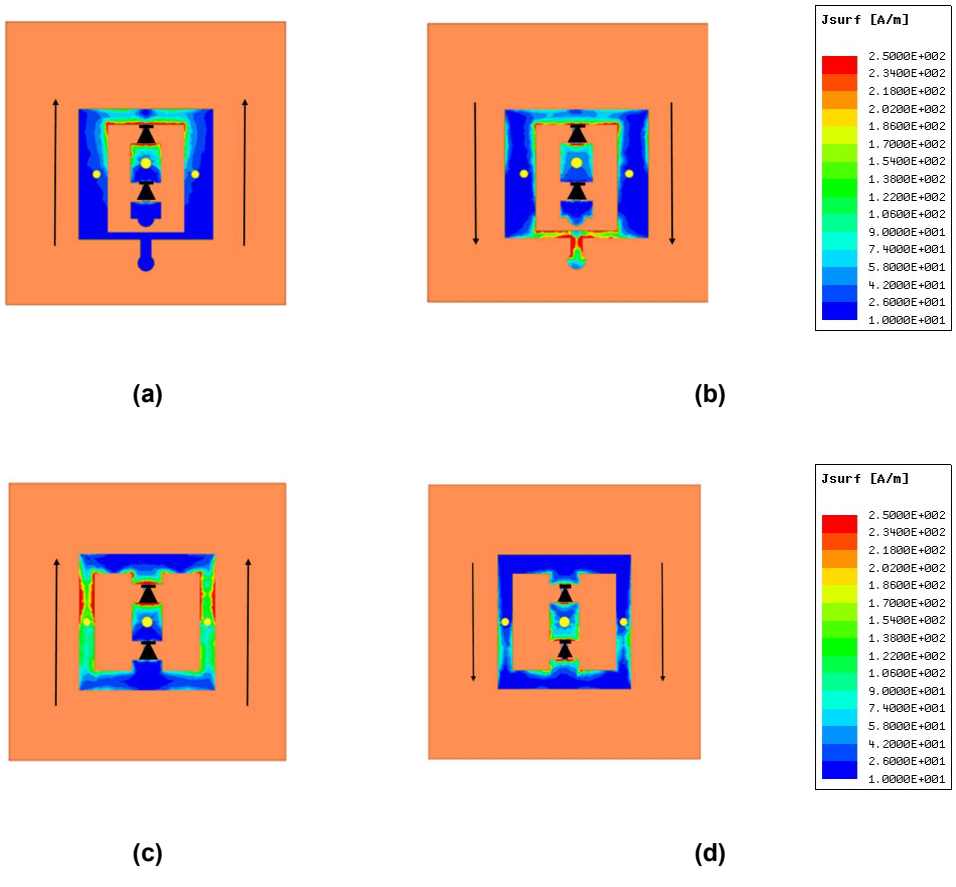

Figure 2-12: Surface currents distributions on the receiving and transmitting patch antennas.(a) Rx-01, (b) Rx-10, (c) Tx-01, and (d) Tx-10.

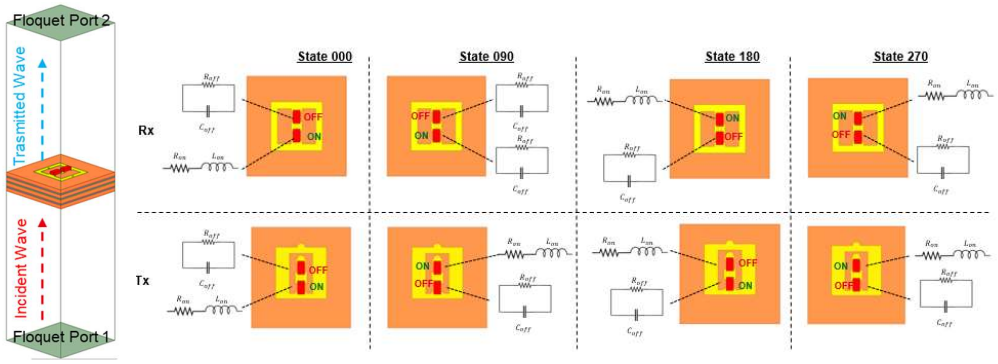

Figure 2-13 Simulation and P-i-N diode states for T-R-UC in 2-bit transmitting mode

The unit cell presents an insertion loss (S_{21}) lower than 2 dB at 29 GHz for all the four different states (Figure 2-12 (b)). The S_{21} levels are acceptable over the frequency band as well as the reflection coefficient magnitudes (S_{11} and S_{22} in Figure 2-12 (a) and (c) respectively). In Figure 2-12 (d) the phase response of the four different states are plotted. These responses demonstrated the capabilities of generating 2-bit phase quantization using the designed unit cell.

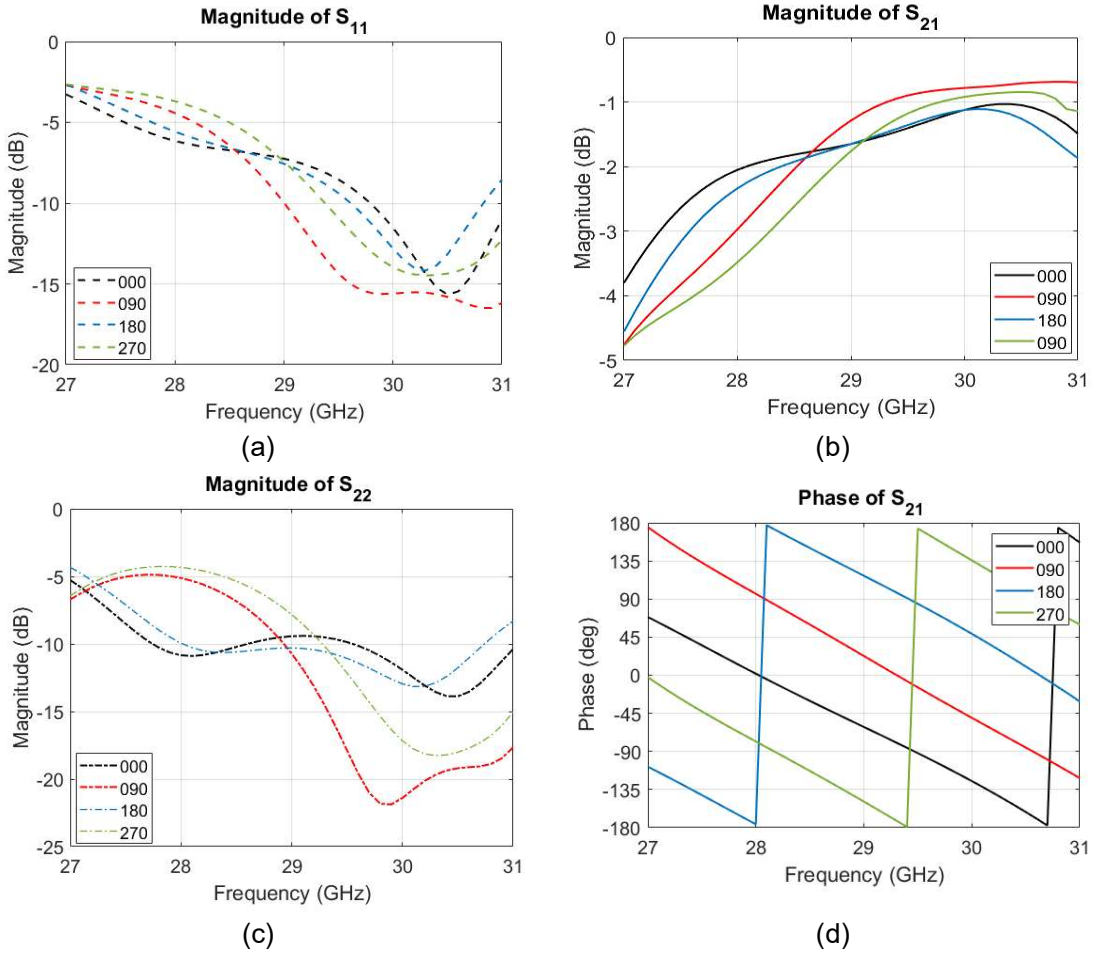

Figure 2-14 S-parameters T-R-UC in 2-bit transmitting mode

The 2-bit unit cell is used in the synthesis of a transmitting RIS. Using an in-house Matlab tool, a 24x24 unit cells RIS is designed and studied. The tool generates the appropriate phase (cell state) distribution respecting a specific pointing angle condition. In Figure 2-12 the radiation patterns in the cut plane $\phi = 0°$ show the capability of the RIS to steer the beam between -60° and +60°. The gain of the beam in broadside is of 28 dBi. The 3D radiation patterns could also be reported for every steering angle (an example is shown in Figure 2-12 (a)).

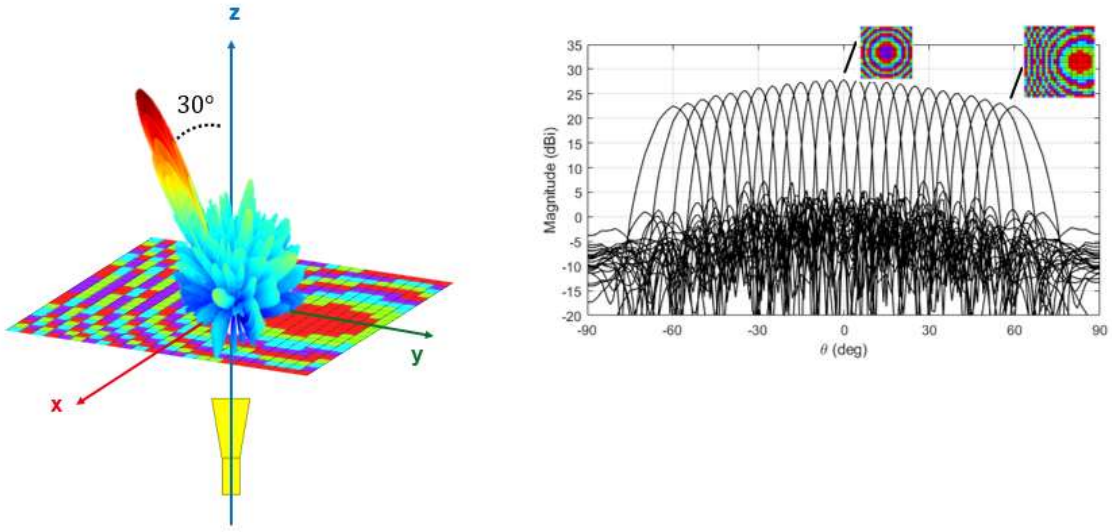

(a) (b)

Figure 2-15 Matlab Simulation of a Transmitive 2-bit RIS of 24x24 unit cells. (a) 3D Radiation Pattern and (b) Steering pattern in the cut plane ϕ=0°.

The synthesized RIS is afterwards prototype in Figure 2-12. The RIS will be characterized and the far field will be measured in an anechoic chamber. An in-house tool is already developed to generate the diodes commands in order to respect a specific phase distribution.

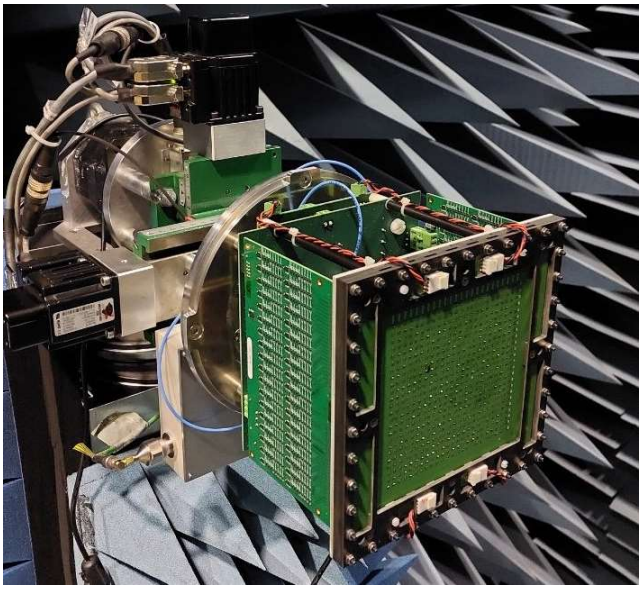

Figure 2-16 The prototype of the Transmitive 2-bit RIS of 24x24 unit cells.

Based on the same topology reported in Figure 2-12, a transmitting/reflecting unit cell is obtained. When both diodes of the Rx-patch are turned off thus the incident wave will be reflected by the Tx-patch directly without being transmitting to the other side of the unit cell Figure 2-12. The alternation of the diodes states (ON/OFF) in the Tx-patch will generate a 1-bit phase quantization this time in reflection. The reflection coefficient magnitude (S_{11}) reported in the Tx-patch side of the unit cell are below -1.5 dB over the frequency band (Figure 2-12). These levels of S_{11} demonstrate the principle of using the same unit cell both in transmission and reflection.

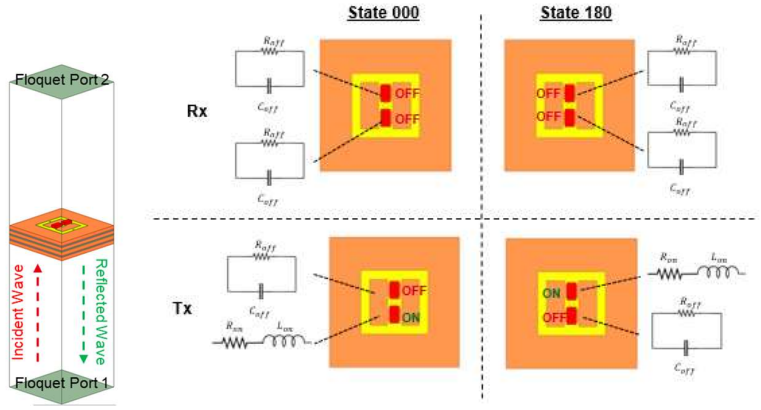

Figure 2-17 Simulation and P-i-N diode states for T-R-UC in 1-bit reflecting mode

In conclusion, the same unit cell is used to synthesize a 2-bit transmitting RIS and a 1-bit reflecting RIS. This architecture could be a strong candidate in the RIS market having both capabilities of transmitting and reflecting the wave within the same surface.

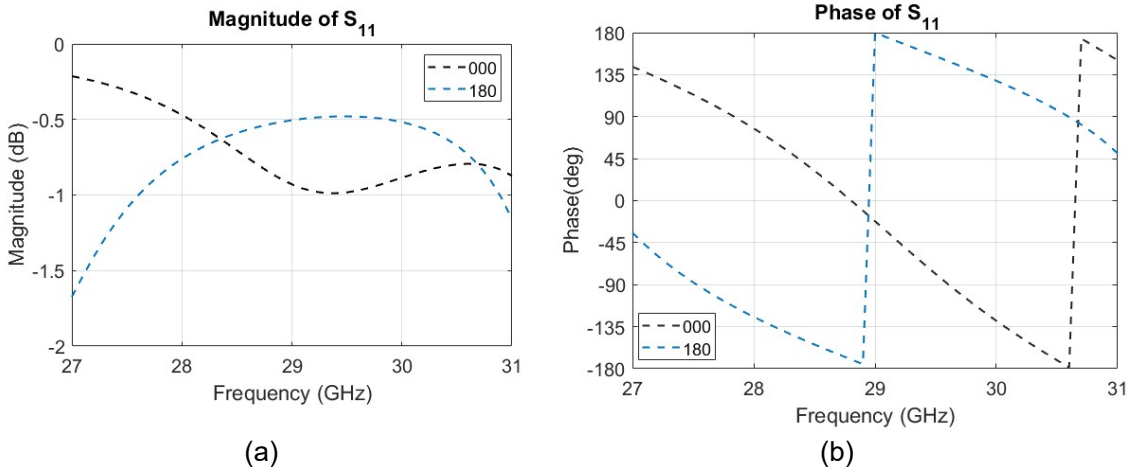

(a) (b)

Figure 2-18 S-parameters T-R-UC in 1-bit reflecting mode

2.2.3 Reflective unit cell RIS design in the Ka band based on PIN diode

The schematic of the proposed linearly-polarized unit-cell is shown in Figure 2-10. It is composed of four metal layers printed on two Isola Astra MT77 substrates (ε_r = 3, tanδ = 0.0017) and bonded with Astra MT77 pre-preg bonding film (ε_r = 2.95, tanδ = 0.0019).The top layer is the radiating element. It consists of center-fed O-slot rectangular patch antenna working in reflecting (Rx) mode. The patch antenna is connected by a metalized via hole located at its center to the ground plane. Two p-i-n diodes MA4AGP907 are flip-chipped on the patch antenna to tune the reflection phase; a bias line printed on the opposite side of the substrate controls them. The patch is also connected to a delay line, printed as well on the opposite side of the substrate. The two p-i-n diodes are biased in opposite states (one p-i-n diode is switched ON while the other one is in OFF state). Due to the presence of the aforementioned delay line a 90° phase-shift ($\Delta\phi$) of the current distributions is obtained. Since the patch is operating in the reflection mode thus the reflection coefficients phase shift is equal to $2x\Delta\phi$ (180°). The bias networks include microstrip radial stubs to isolate the RF signals. The DC connection to ground is realized with a short circuit stub.

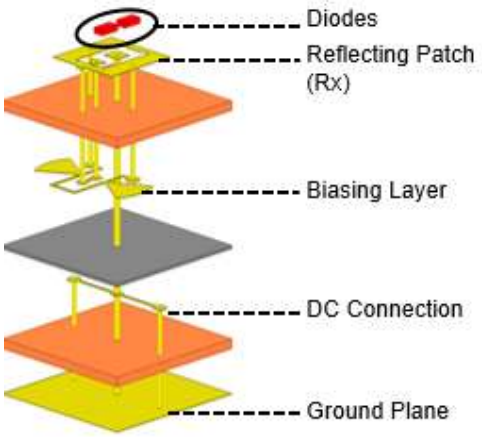

Figure 2-19 Schematic view of the Reflecting RIS unit cell

The two generated states of the unit cells will be referred to as the following: State000 and State180. This 1-bit unit-cell has been simulated for its two-phase states using the commercial software Ansys HFSS with periodic boundary conditions on the unit-cell lateral faces and Floquet port excitation as already explained in the previous section. The unit cell presents a phase difference of almost 180°± 20° (the red curve labeled “old” in Figure 2-10 (b)). The reflection coefficient magnitude is smaller than 2dB over the frequency band for both unit cell states (the red curve labeled “old” in Figure 2-10 (a).

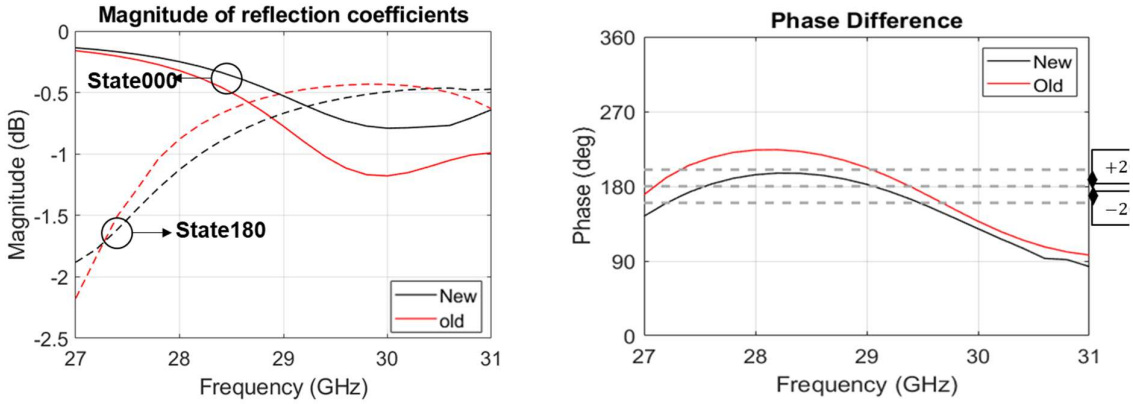

(a) (b)

Figure 2-20 S-parameters Reflecting UC

The 1-bit unit cell is used in the synthesis of a reflecting RIS. In order to synthesize and simulate the reflecting RIS, an updated Matlab tool is developed in order to consider the reflection scenario. Using the Matlab tool, a 20 x 20 unit cells RIS is designed and studied. In Figure 2-12 the radiation patterns in the cut plane $\phi = 0°$ show the capability of the RIS to steer the beam between -60° and +60°. The 3D radiation patterns could also be reported for every steering angle (an example is shown in Figure 2-12 (a)).

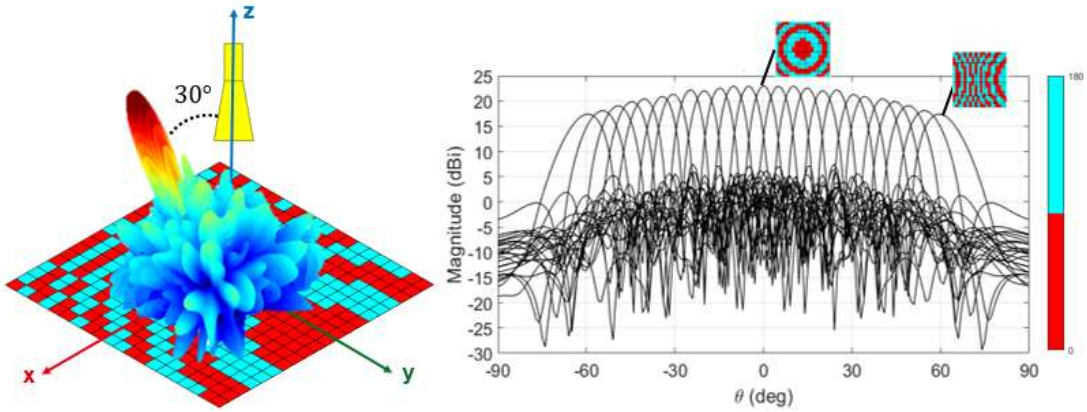

(a) (b)

Figure 2-21 Matlab Simulation of a Reflecting 1-bit RIS of 20x20unit cells. (a) 3D Radiation Pattern and (b) Steering pattern in the cut plane ϕ=0°.

A full wave simulation of a reflecting 1-bit RIS using Ansys HFSS is made, for the sake of validation of the developed Matlab Tool. The size of the RIS is set to 8x8 unit cells (D = 8 x 5.1 mm = 40.8 mm) and the horn is positioned at a focal F (with F/D = 0.8). The validation could be done for larger RIS but this would be time consuming. The phase compensation is generated in order to steer the beam towards -10° direction. This is set to prevent the shadowing caused by the horn position (in the middle of the RIS). In Figure 2-12, we can see a good agreement in the radiation pattern between the Matlab simulation (blue curve) and the HFSS simulation (black curve).The side lobe levels are higher and the maximum gain is slightly lower, in the case of HFSS since the physical size of the horn is big compared the RIS one; and thus the horn shadowing is taken more into consideration in the full wave simulation.

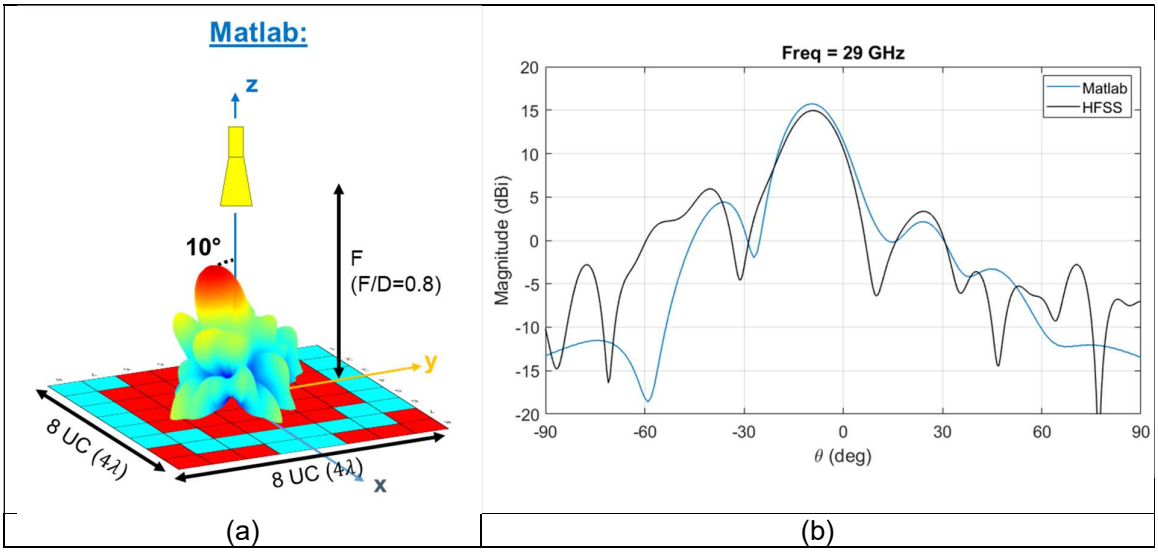

Figure 2-20 (a) Hybrid Matlab Simulation of relfecting RIS, (b) comparaison with full-wave simulation in HFSS in the cut plane ϕ=0°.

In conclusion, the unit cell performances are encouraging and the Matlab tool is validated even for a small size RIS. In the meantime, a reflecting 1-bit RIS of 20x20 unit cells is designed and should be prototyped and measured (Figure 2-12 (b)). In order to fabricate the RIS, the command lines of the diodes are as well designed. The unit cell 3D schematic shown in Figure 2-12 (a), present the complete design. A layer of Isola Astra MT77 substrate is bonded using Astra MT77 pre-preg bonding film on the bottom, thus the command lines will be printed on each side. The complete unit cell (Figure 2-12 (a)) is simulated using periodic boundary conditions and excited with a Floquet port on Ansys-HFSS. The unit cell performances in terms of reflection coefficient magnitudes and phase difference are presented in Figure 2-12 (a) and (b) respectively. The RIS will be afterwards, characterized and measured in an anechoic chamber.

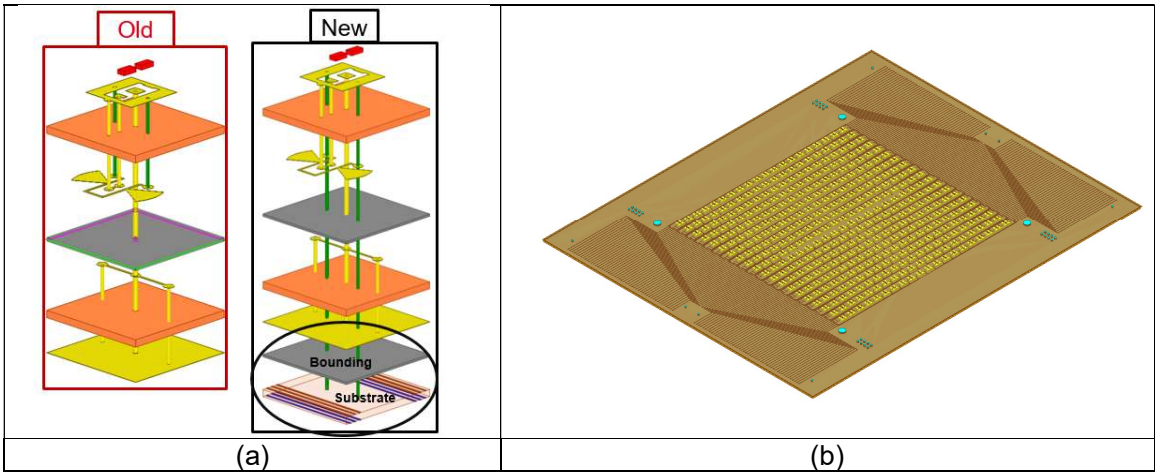

Figure 2-23 (a) Unit cell updates: introduction of command lines layers, (b) 3D sketch of the prototype of a Reflecting 1-bit RIS of 20x20 unit cells.

2.2.4 Sub-6GHz RIS based on MEMS technology : numerical design

The RIS design consists of an 8x8 array of dual-polarized patch elements. The full 8x8 array is partitioned into 4 segments with 4x4 patches sharing a control board, one such segment is shown in Figure 2-21. Partitioning allows for higher flexibility during production, and allows for experimenting with spacing between the elements. The array is designed to operate in the 3.6—3.8 GHz band.

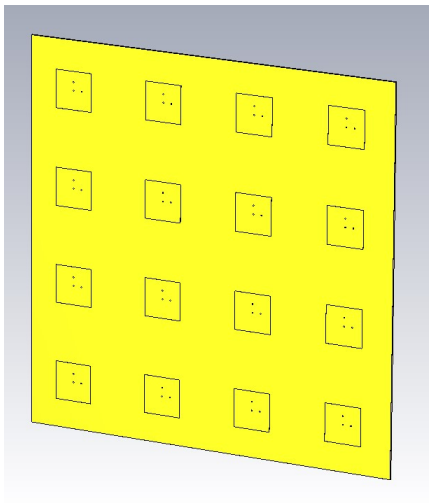

Figure 2-21 – 4x4 segment of the reflective RIS array at 3.7 GHz.

Detail of the patch scattering element used as a unit cell in the CST simulations is shown in Figure 2-22. To improve on efficiency, the patch is printed on the back side of a low-loss F4BM substrate (not shown in Figure 2-21 and Figure 2-22), so that there is an air gap between the patch and the ground plane. The ground plane is on the front side of a FR-4 substrate whereas the two RIS loads, one for each polarization, are placed on its back.

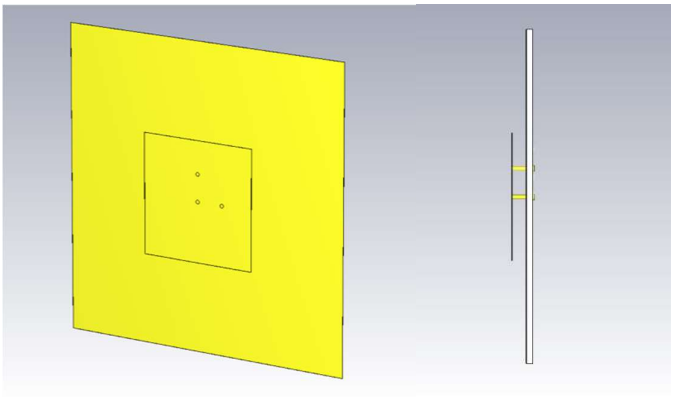

Figure 2-22 – Detail of the array element unit cell; circles show the feeding points of the patch.

The array has been modeled in CST Microwave Studio using the unit cell approach in two directions and tetrahedral mesh F-solver. The unit cell is excited by an incident wave from the front while the reflection coefficient of the load is varied through four points on the outer rim of the Smith chart. Figure 2-23 shows the backscattering/reflection coefficient of the vertical polarization (horizontal has similar properties) magnitude and phase.

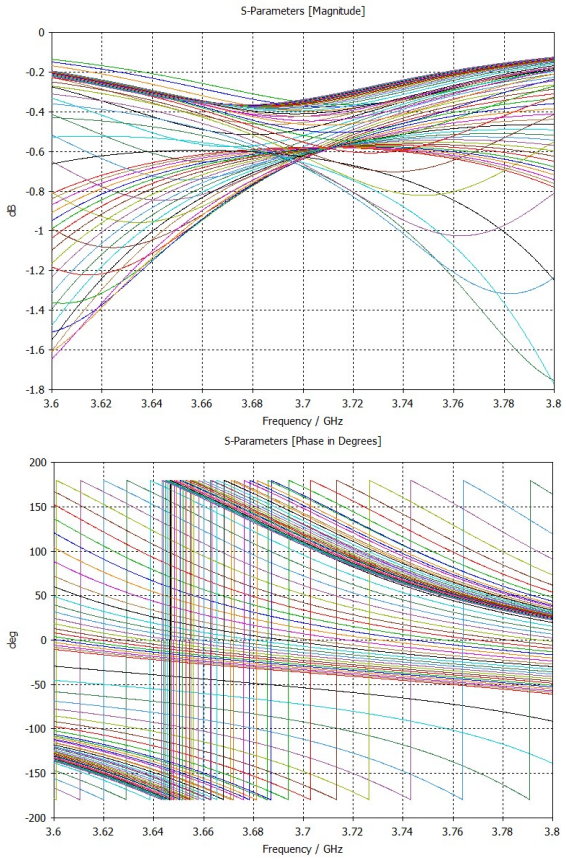

Figure 2-23 – Reflection coefficient magnitude (left) and phase (right) of the boresight incident wave for various phase shifter settings.

The insertion loss of the unit cell is within 2 dB in the desired frequency range 3.6—3.8 GHz for selected phase shifter settings, whereas the phase covers the entire 360° domain.

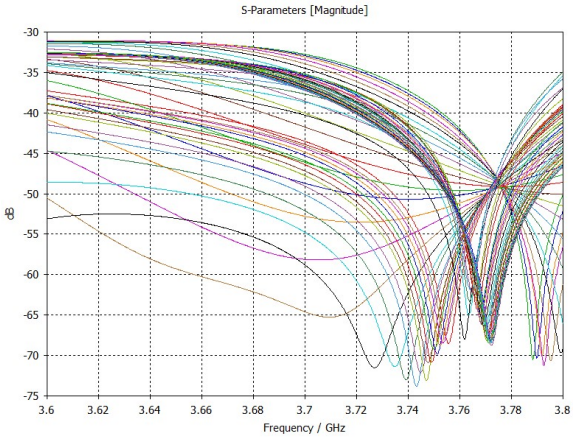

Figure 2-24 – Cross-polarization coupling between boresight incident and reflected waves for various phase shifter settings.

The RIS array should also operate independently for both polarizations, which can be seen in Figure 2-24 – the cross-polarization of the scattered wave in boresight is below -30 dB in the entire frequency band.

The loads for each polarization will consist of reflective phase shifters, each with two MEMS capacitors having 5-bit control range. The control board should be common for the 4x4 building block of the array, with daisy-chaining of all the blocks in the entire array. Preselected values of the capacitors will be stored in a non-volatile memory placed on board, allowing for fast switching via lookup tables.

2.2.5 Sub-6GHz RIS design based on RF switches

The high-level view of the proposed RIS design is shown in Figure 2-25. On the left-hand side the entire array is a square with sides of length 272.54 mm and composed of 10x10 unit cells. Each unit cell has dimensions 19.4 x 15.97 mm (right-hand side) and consists in a patch antenna and a feeder line.

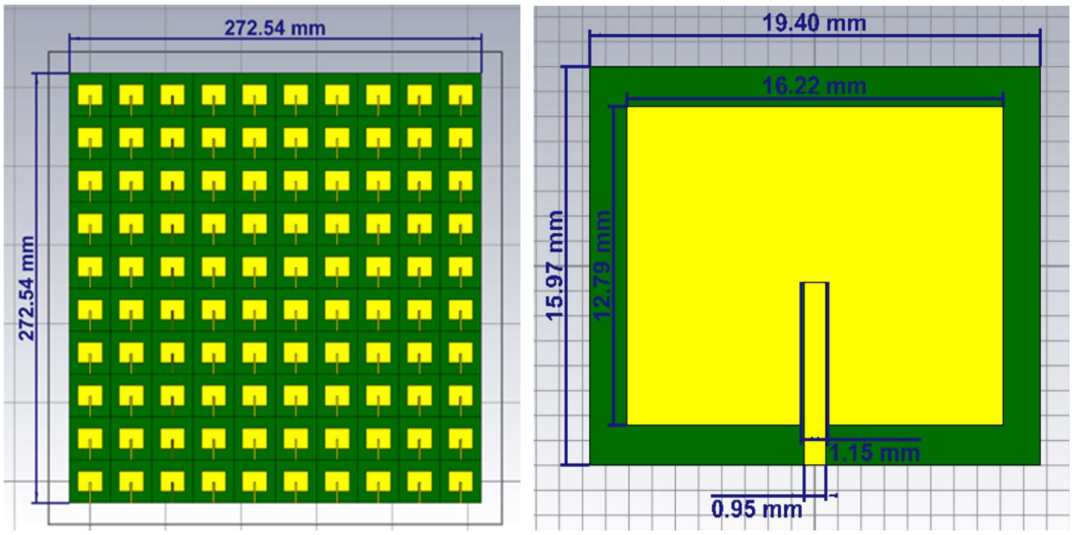

Figure 2-25: Proposed 10x10 RIS design (left-hand side) and associated unit cell (right-hand side) at 5.3 GHz.

The inter-element spacing is fixed at half the operating wavelength. Such value is chosen to strike a trade-off between increasing the number of RIS elements in the same physical space and avoiding unwanted array non-idealities, such as mutual coupling or grating lobes, as depicted in Figure 2-26, for the case of a 10x10 RIS array at 27.96 GHz.

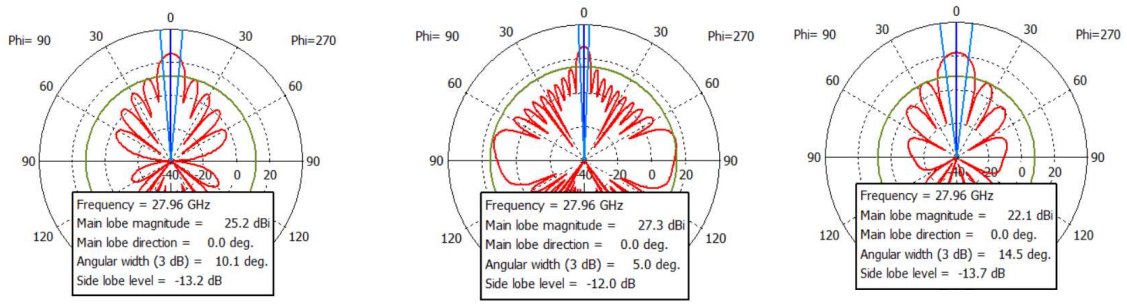

Figure 2-26: Array response for a 10x10 RIS with different inter-element spacing.

Each unit cell is designed to operate at 5.3 GHz as shown in Figure 2-27. Here, we compare the full-wave simulation in CST with measurements operated with a VNA. The offset from the theoretical simulation to the experimental measurement is due to an error in the nominal permittivity used in the simulations of the PCB substrate.

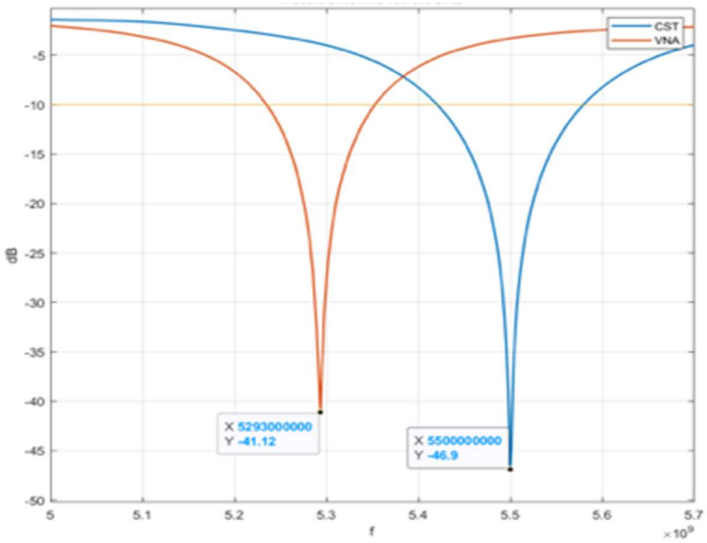

Figure 2-27: S11 parameter of the proposed RIS unit cell.

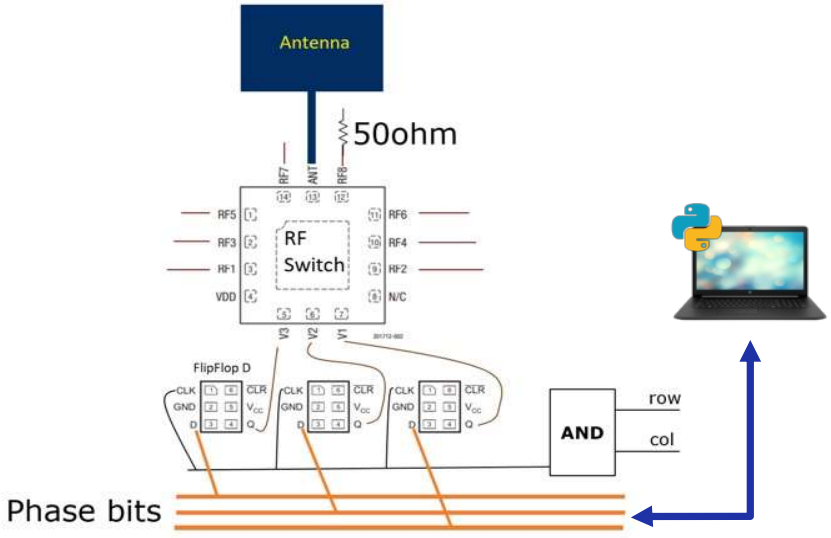

Figure 2-28: Schematic of each RIS unit cell.

As shown in Figure 2-28, each patch antenna in the array is connected to an 8-port RF-switch, which is used to obtain the phase-shifting capability. Indeed, each output port feeds an open-ended transmission line of a specific length, thereby adding a delay to the incoming signal and hence generating the desired phase-shift.
All unit cells are connected to a central MCU, which is in charge of communicating the chosen configuration in terms of phase-shifting capability via ad-hoc communication buses embedded in the PCB. In particular, we use 3 FlipFlop D to select one out of the eight available transmission line outputs. Moreover, one of the aforementioned output ports of the RF switch is connected

to a 50 Ω resistor, which is used for debugging purposes. The final printout is shown in Figure 2-29 (left-hand side).

Experimental validation of the proposed RIS design is currently undergoing. In particular, as depicted in the right-hand side of Figure 2-29 we are exploiting an 8 x 5 m anechoic chamber, where we place the TX, namely a USRP connected to a horn antenna, in the vicinity of the RIS and at a fixed angle. On the other side of the chamber, we place a receiver, i.e., a horn antenna connected to a USRP, on a rotating platform. The latter allows us to verify the received power not only for different RIS configurations, but also for different receiver locations.

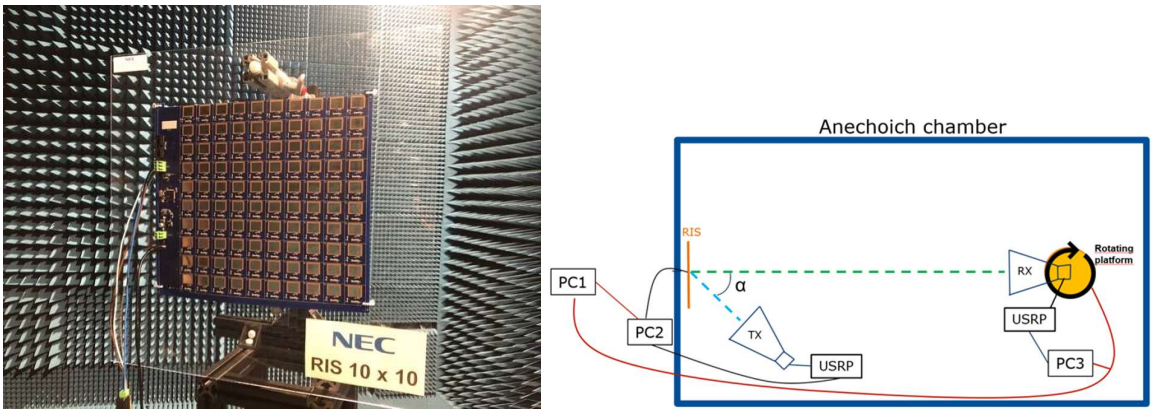

Figure 2-29: Anechoic chamber measurement setup.

2.2.6 Varactor characterisation for integration in the numerical design of a reflectarray in Ka band

After a first iteration in the design of the Ka band controllable unit cell to evaluate the RF performance and the reflection phase excursion, a stage of characterization has been done to evaluate experimentally the varactor diodes chosen from the manufacturer datasheet to reduce as much as possible the gap between simulated et measured RF performance of the controllable surface. This validation stage will allow to extract from the scattering matrix measurements an RLC equivalent circuit of the varactor diode to be used in the EM simulators.

The varactor diodes have been tested on a coplanar line (Figure 2-30 (c)). A universal test fixture (Figure 2-30 (b)) has been used with DC blocks on each side to isolate RF signal to DC currents on the network analyser (Figure 2-30 (a)). A Coplanar Line TRL calibration has been done with 3 coupons (Reflect, Thru and Line @ 30 GHz) (Figure 2-30 (d)) before the S matrix measurements for several inverse voltages applied on the varactor diodes.

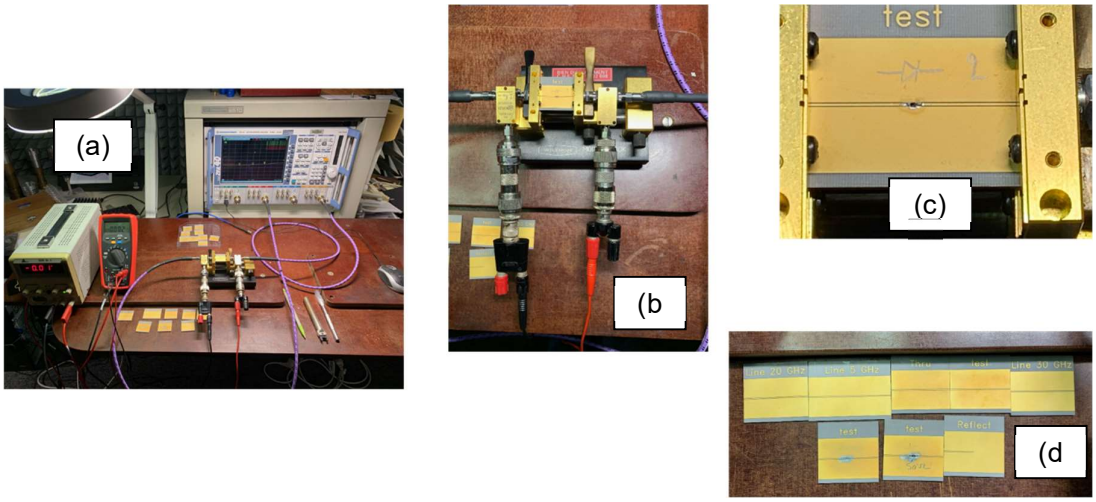

Figure 2-30 – varactor diodes test bed

Scattering matrix measurements have been done between 22.0 GHz to 30.0 GHz with the inverse voltage varying between 0.0 V to 19.0 V with a step of 0.1 V from 0.0 to 7.0 V, a step of 0.2 V from 7.2 V to 10.0 V and 0.5 V from 10.5 to 19.0 V.

From these measurements, an extraction of the RLC values (Figure 2-31 (b)) of the varactors diodes equivalent circuit (Figure 2-31 (a)) has been done.

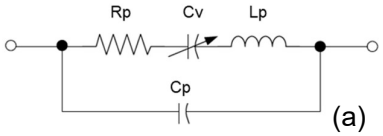

(a)

$$Ztot := -\frac{I\left(Rp + I\,\omega\,Lp - \frac{I}{\omega\,Cv}\right)}{\omega\,Cp\left(Rp + I\,\omega\,Lp - \frac{I}{\omega\,Cv} - \frac{I}{\omega\,Cp}\right)} = Rz + I\,Iz$$

(b)

Figure 2-31 – RLC equivalent circuit (a) – RLC equivalent impedance (b)

The RLC values of the equivalent circuit correspond to:

- Cv variable capacitance of the varactor diode,
- Cp parasitic capacitance of the package,
- Lp parasitic inductance of the package (bounding),
- Rp parasitic resistance of the package (bounding).

To start the extraction, the Lp and Cp values are static and has been fixed from the package type of the diode. Then Cv and Rp are extract from the Ztot formula (Figure 2-31 (b)).

After the TRL calibration, discrepancies on Sij measurements (Figure 2-32) are observed above 24.0 GHz that affect the RLC value extraction with for example negative values of Rp that are not consistent with passive component.

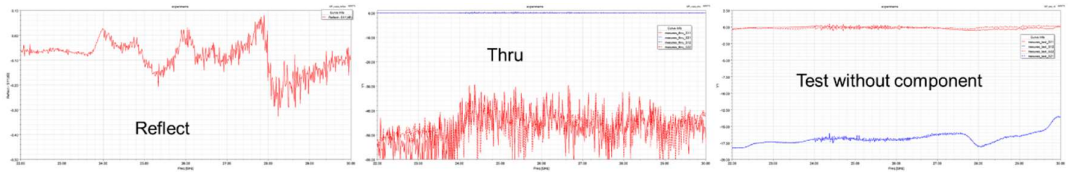

Figure 2-32 – measured Sij on TRL kit coupons

A reduced frequency range (up to 24.0 GHz) has been used for the RLC values extraction, and a tuning of the parasitic components (Rp, Lp, Cp) has been done to obtain Cv curves depending on the inverse voltage identical for several frequencies (Figure 2-33). The measured S matrixes aren't not completely symmetric, so extractions have been done from S11 (Figure 2-33 (a)), S22 and an average after symmetrisation (Figure 2-33 (b)).

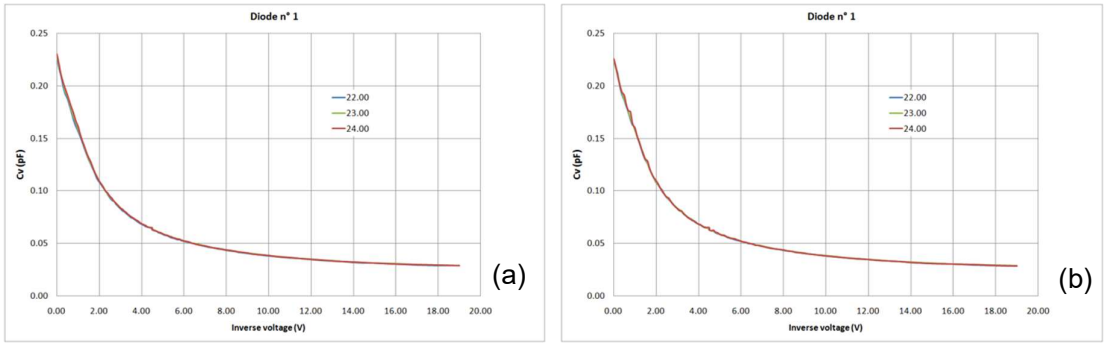

Figure 2-33 – Cv curves from S11 (a) and averaging (b) @ 22.0, 23.0 and 24.0 GHz

With Lp = 0.15 nH, CP = 0.015 pF and Rp = 7.5 Ω, the curved presented for the 3 frequencies are in good agreement and the average gives identical excursion. The extraction of Cv gives a capacitance variation from 0.23 pF with 0.0 V applied on the diode to 0.03 pF for 19.0 V. These values agree with the datasheet (0.19 pF < Cvmax < 0.275 pF) and (0.025 pF < Cvmin < 0.038 pF).

Then a phase of comparison between simulations and experiments has been done. The coplanar line with the diode has been simulated with the extracted RLC values (Figure 2-34). And the measured and simulated S11 are compared (Figure 2-35). Completely different behaviour can be observed with a HFSS simulations but also with other commercial EM software's.

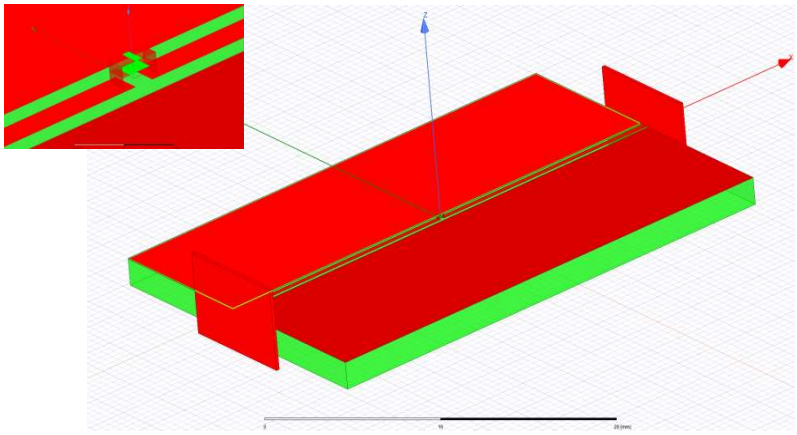

Figure 2-34 – Model of the simulated coplanar line with RLC circuit diode

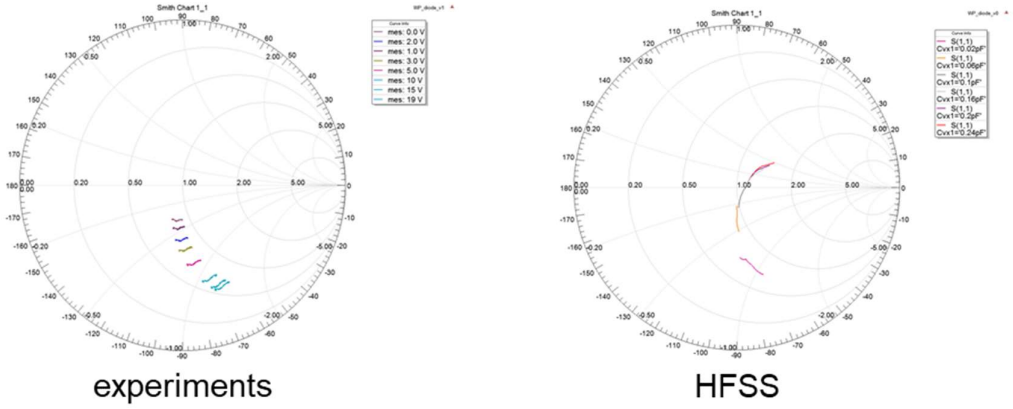

Figure 2-35 – comparison of simulated and measured S11

Currently, the discrepancies on Smatrix measurements above 24.0 GHz and the gap between simulations and experiments on Smatrix comparisons are under investigation before to start the fine tuning of the unit cell to provide for manufacturing.

2.2.7 Hybrid reflecting and sensing RIS design based on varactor.

The proposed HRIS is reflective with integrated sensing capabilities, meaning that small portions of the incident wave are coupled to an array of sensing waveguides.
The elements of the proposed HRIS are mushroom structures as shown in Figure 2-36 each loaded with a varactor diode which acts as a reconfigurable capacitance that controls the resonance frequency and consequently the effective impedance. An annular slot separates the via from the ground plane beneath the substrate, allowing for coupling of the incident wave to another layer. This annular slot is taken advantage of to sense the incident wave. The diameter of the annular slot and the characteristic dimensions of the coupling waveguide control the amount of coupling and consequently the portion of the incident wave that is being sensed at the meta-atom. The primary criterion in designing the proposed meta-atom is to ensure a small portion of the incident wave can be sensed while maintaining sufficient reflective power and a reconfigurable reflective phase (to form desired reflection patterns). For guiding the sampled signal, Substrate Integrated Waveguides (SIWs) are used because they do not couple to each other, spurious radiation is avoided at the junction with the via, and by tweaking the distance from the via to the sides of the SIW and/or changing the cut-off frequency of the SIW, the coupling between the SIW and the meta-atom can be further tailored.
The meta-atom has been simulated in Ansys HFSS in the setup shown in Figure 2-37a. The dielectric substrate has been assumed to be RO4003 with relative permittivity of 3.55 and a loss tangent of 0.0027. The varactor is modeled as a lumped element with a variable capacitor. The hardware dimensions are optimized for the operation to be at around $19\ GHz$ are shown in Figure 1 and can be easily modified to facilitate other operating frequencies. The element size and the spacing between elements have been designed to be around a quarter of the wavelength balancing between better accuracy of the desired reflected beams and large inter-element coupling and fabrication cost that comes with smaller inter-element spacing.
The reflection from the meta-atom and the coupling to the SIW can be examined through the scattering parameters S_{11} and S_{21} respectively. In Figure 2-37 b and c, the simulated scattering parameters are presented, using the simulation setup of Figure 2a. The diameter of the via and the annular slot are respectively $0.5\ mm$ and 0.6 mm, the SIW dimensions are $8.7\ mm \times 4\ mm \times 1.5\ mm$, and the distance between the via and the shorted edge of the SIW is $1.6\ mm$. The via is equidistant from the other two side walls of the SIW. In Figure 2-37 (b), it is evident that the

coupled signal $|S_{21}|$ is below $-15\ dB$ for the whole frequency range while the magnitude of the reflection coefficient $|S_{11}|$ is above $-2.5\ dB$ and is maintained such for a range of varactor capacitanes in Figure 2c. This result satisfies the primary meta-atom design criterion. In Figure 2-37 (c), the phase of S_{11} in radians is depicted versus a range of varactor capacitances in pF.

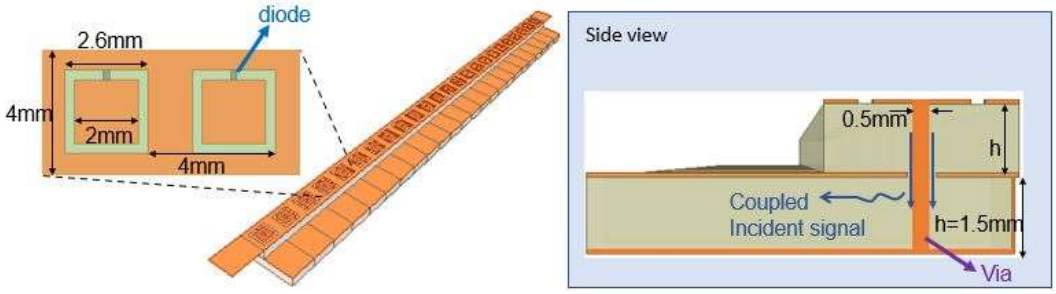

Figure 2-36 Hybrid RIS hardware design with integrated sensing capability.

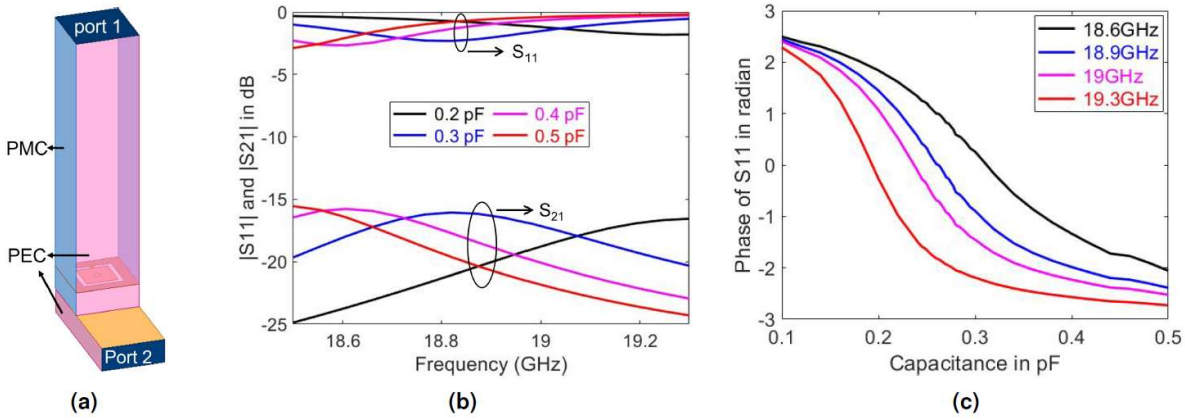

Figure 2-37 a) The simulation setup used for the hybrid meta-atom. b) Simulated reflection $|S_{11}|$ and coupling $|S_{21}|$ as a function of operation frequency. c) Phase of S_{11} as a function of the varactor capacitance at several frequencies.

In order to demonstrate that the sampled signal at the previously designed meta-atoms contains information about the impinging signal, a 1D array of 24 such meta-atoms (periodic along the Y axis) has been simulated, as shown in Figure 2-38. The intention is to show that the proposed structure can infer the direction of the incident beams and steer them in the XZ-plane. To estimate the Angle of Arrival (AoA) of an impinging signal, a comparison between the differential phase (phase differences between adjacent elements) of an unknown incident beam with a set of pre-recorded measurements. In Figure 2-38, the phase differences for four incident angles are depicted for each measurement index (index I refers to the adjacent meta-atoms I and i+1). It is observed that the phase difference is not constant across the elements for the same incident angle, and this is caused by coupling between the elements and scattering of the waves in the substrate. Also, the phase differences change for different AoAs. In Figure 2-38 c , the averaged over 10 realizations accuracy η (defined in a binary fashion $\eta = 1$ when the difference between the estimated and the actual AoA is less than 2.4° or else $\eta = 0$) is presented as a function of the Signal to Noise Ratio(SNR) level, for four AoAs. It is observed that the AoA can be recovered, verifying the proposed design and operation.

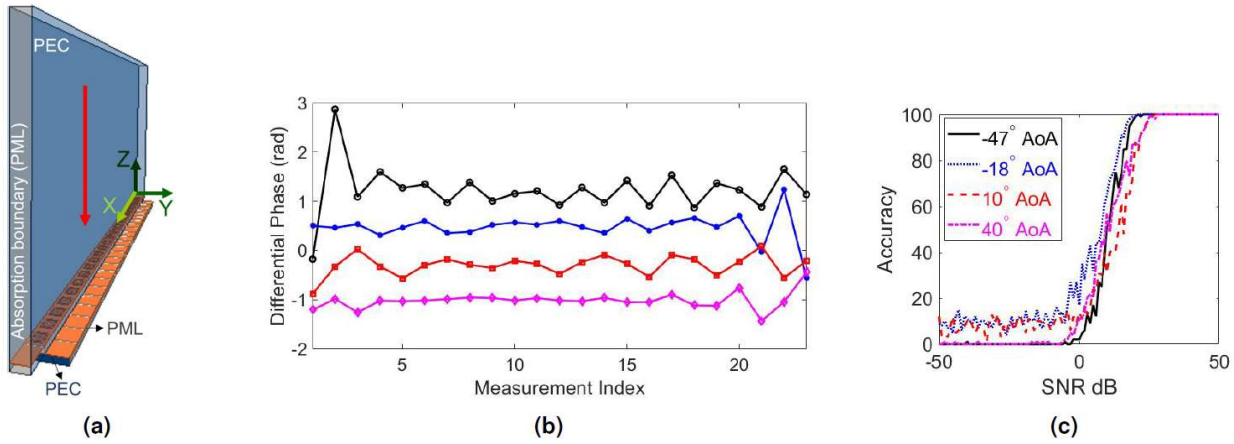

Figure 2-38 a) The setup for illuminating the RIS with a Gaussian beam. The red arrow indicates the normal incidence. PML refer to perfectly matched layer. b) Differential phase along the 1D metasurface array for four different incident angles captured inside SIWs. c) AoA estimation accuracy (in percentage) as a function of the signal-to-noise ratio (SNR). The incident angles are the same in both plots.

2.2.8 RIS Unit Cells design in the D-band

A D-band integrated circuit (IC) is designed, fabricated using 130nm Infineon SiGe BiCMOS process. The IC represents a single elements in RIS UC. The diagram of the D-band IC design is shown in the figure below.

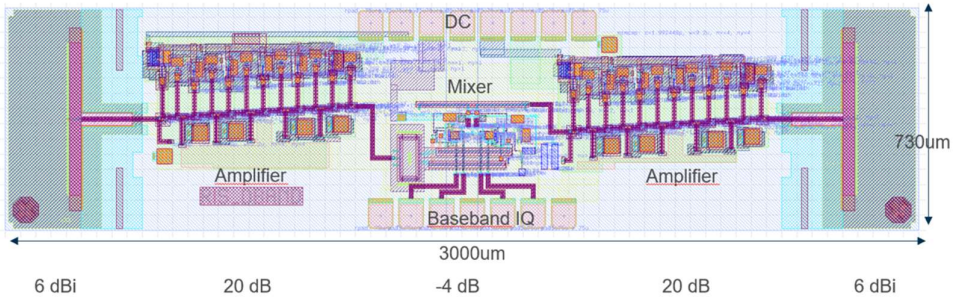

Figure 2-39 D-Band IC design

The fabricated IC measured as 730 µm x 3000 µm in size, and it comprises of antenna, amplifier and mixer modules all integrated on single chip. The antenna when used has 6 dBi directivity, and the amplifier in used has 20 dB small signal gain and bandwidth covers 120-169 GHz. The mixer takes input from one antenna and provided phase shift to this signal then output using the other antenna. The phase shift is applied by setup baseband IQ path voltage and such IQ path has modulation bandwidth over 20 GHz.

The simulated antenna performance is also illustrated below which shown radiation pattern at 150 GHz.

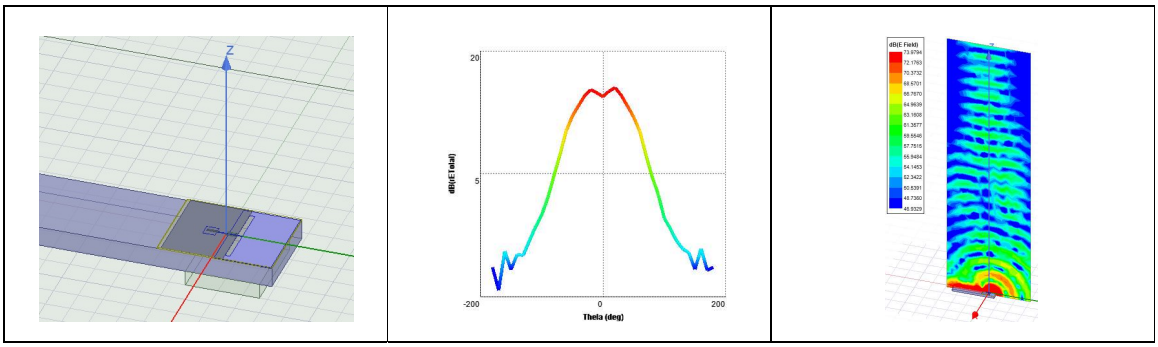

Figure 2-40 UC performance in D-Band

When several such ICs are placed on a carrier board to form a RIS array, by adjusting baseband voltage of each element the reflection profile of D-band RIS can be controlled.

3 Conclusions and perspective

In the table here below we list the status of main RIS design, concept and prototypes. Part of them could fulfil the requirements for a demo but precise alignment with the PoC requirements, especially with respect to the bands, are expected for final RISE-6G design. The green color is used when the characterisation have been already done and orange one when the characterisation is on-going. In the label product in the column prototype mean that the RIS design is almost ready for industry and it can be manufactured quickly in a required number of samples with a plug and play interface.

Within WP3 context, RIS prototypes will be used to validate models proposed in D3.1 and to perform experimental RIS Radio Environment Sounding (T3.3).

With respect to other WP of the project, some of the RIS in Table 3-1 have already been used for the demo presented in D7.1 of WP7. For instance one of the demo in D7.1 leverage the Greenerwave RIS packaged as mmW access point extender (Figure 2-7) to demonstrate how RIS technology allows one to restore a data transmission between two antennas in the NLOS situation and establish a solid mmW communication channel in a real complex indoor environment such as an office (Figure 2-8). Indeed at mmW a signal from a base station experiences significant fading due to propagation loss and shadowing by buildings, landscape or indoor walls.

In addition, in the coming months, the partners will also consider how to optimally integrate and use some of the designs presented in this deliverable in field trials of T7.2 and T7.3. This work will merge all together the RIS prototypes and models from WP3 but also the methods from WP4-6 (D4.2, D4.3, D4.4, D5.2, D5.4, D6.2, D6.4) and the architectures from WP2 (D2.5),

Table 3-1 RISE-6G prototypes and concepts

	Key parameters						Unit cells design and characterization		RIS	control board	prototyp
GW-1	Reflective binary	5.2 GHz	500 MHz	double pol	λ/2	Pin diode	Num	Exp	28cmx23cm - 76x2 elements	Usb interface- Python+Matlab	product
GW-2	Reflective binary	28 GHz	>3 GHz	double pol	λ/2	Pin diode	Num	Exp	10 cmx10cm 15 cm x 15 cm	FPGA based, Usb + Ethernet interface- Python+Matlab	product
GW-3	Reflective binary	28 GHz	>3 GHz	double pol	λ/2	Pin diode	Num	Exp	10 cmx10cm 15 cm x 15 cm 20cm x20 cm	FPGA based, Usb + Ethernet interface- Python+Matlab	product
GW-4	Reflective binary	28 GHz	>3 GHz	double pol	λ/2	Pin diode	Num	Exp	10 cmlx 10 cm 15 cm x 15 cm 20cm x20 cm	FPGA based, Usb + Ethernet interface- Python+Matlab	product
GW-5	Reflective/ binary	3.6GHZ	>500 MHz	double pol	λ/2	Pin diode	Num	Exp	28cmx23cm	Usb interface- Python+Matlab	product
GW-6	Reflective/or Transmitive binary	3.5 Ghz	-	single pol	λ/2	Pin diode	Num	Exp	-	Python+Matlab	proto

CEA-1	T-RIS 1-bit	X	1.8 GHz	Single LP	λ/2	Pin di-ode	Num	Exp	30cmx30cm 400 elements	Usb inter-face µcon-troller Matlab	Proto
CEA-2	T-RIS 1-bit	Ka	> 3 GHz	Dual CP + Dual LP	λ/2	Pin di-ode	Num	Exp	10cmx10cm 400 elements	Usb inter-face µcon-troller Matlab	Proto
CEA-3	T-RIS 1-bit	Ka	8 GHz	Single LP	λ/2	Pin di-ode	Num	Exp	10cmx10cm 400 elements	Usb inter-face µcon-troller Matlab	Proto
CEA-4	T-RIS 2-bit	Ka	> 3 GHz	Single LP	λ/2	Pin di-ode	Num	Exp	7cmx7cm 196 elements	Usb inter-face µcon-troller Matlab	Proto
CEA-5	T-RIS 2-bit	Ka	> 2 GHz	Dual CP + Dual LP	λ/2	Pin di-ode	Num	Exp	120cmx120cm 576 elements	Usb inter-face µcon-troller Matlab	Proto
CEA-6	T-RIS 2-bit R-RIS 1_bit	Ka	> 3 GHz	Single LP	λ/2	Pin di-ode	Num	-	120cmx120cm 576 elements	Usb inter-face µcon-troller Matlab	Proto Change of control board
AAu-1	Reflective	3.7 GHz	200 MHz	double pol	λ spac-ing	MEMS	Num	-	-	segments with 2x2 patches sharing a control board	proto
ORA-1	Reflective (con-tinous phase)	25.8GHz	3.25 GHz	single pol	-	Varac-tor	Num	Exp		Under dev.	proto
ORA-2	Reflec-tive(con-tinous phase)	5,5 GHz	0,8 GHz	single pol	-	Varac-tor	Num	Exp		RA ready. Logic con-trol under test	proto

NEC	Reflective 3-bits	5.3 GHz	-	Single pol	λ/2	Patch anten-nas	Num	Exp	27.2 x 27.2 cm	MCU	Proto

4 References

[AAS14] L. R. Arnaut, M. I. Andries, J. Sol and P. Besnier, "Evaluation Method for the Probability Distribution of the Quality Factor of Mode-Stirred Reverberation Chambers," in IEEE Transactions on Antennas and Propagation, vol. 62, no. 8, pp. 4199-4208, Aug. 2014, doi: 10.1109/TAP.2014.2327642.

[AAS21] I. Alamzadeh, G. C. Alexandropoulos, N. Shlezinger, and M. F. Imani, "A re-configura-ble intelligent surface with integrated sensing capabilities," Springer Nature Scientific Re-ports, to appear, 2021.

[AAT16] V. S. Asadchy, M. Albooyeh, S. N. Tcvetkova, A. D¡az-Rubio, Y. Ra'di, and S. A. Tretyakov, "Perfect control of re-flection and refraction using spatially dis-persive metasurfaces," Phys. Rev. B 94, 075142 - 19 August 2016.

[ADD21] A. Abrardo, D. Dardari, M. Di Renzo and X. Qian, "MIMO Interference Chan-nels Assisted by Reconfigurable Intelligent Surfaces: Mutual Coupling Aware Sum-Rate Optimization Based on a Mutual Impedance Channel Model," in IEEE Wireless Communications Letters, vol. 10, no. 12, pp. 2624-2628, Dec. 2021.

[AG12] L. R. Arnaut and G. Gradoni, "Probability Distribution of the Quality Factor of a Mode-Stirred Reverberation Chamber," in IEEE Transactions on Electromag-netic Compatibility, vol. 55, no. 1, pp. 35-44, Feb. 2013.

[AG15] L. R. Arnaut and G. Gradoni, "Probability Distribution of the Coherence Band-width of a Reverberation Chamber," in IEEE Transactions on Antennas and Propagation, vol. 63, no. 5, pp. 2286-2290, May 2015.

[AKG15] K. Achouri, B. A. Khan, S. Gupta, G. Lavigne, M. A. Salem, and C. Caloz, "Synthesis of electromagnetic metasurfaces: principles and illustrations", EPJ Applied Metamaterials, vol. 2, p. 12, 2015.

[ARA19] B. Addissie,J. Rodgers, T. Antonsen, “Extraction of the coupling impedance in overmoded cavities,” Wave motion, Apr 1;87:123-31, 2019.

[ASA21] G. C. Alexandropoulos, N. Shlezinger, I. Alamzadeh, M. F. Imani, H. Zhang, and Y. C. Eldar, "Hybrid reconfigurable intelligent metasurfaces: Enabling sim-ultaneous tunable reflections and sensing for 6G wireless communications," [Online] https://arxiv.org/pdf/2104.04690.pdf, 2021.

[ASC151] K. Achouri, M. A. Salem, and C. Caloz, "General metasurface synthesis based on susceptibility tensors", IEEE Trans. Antennas Propag., vol. 63, no. 7, pp. 2977-2991, Jul. 2015.

[ASC152] K. Achouri, M. A. Salem, and C. Caloz, "Electromagnetic metasurface perform-ing up to four independent wave transformations", in 2015 IEEE Conference on Antenna Measurements Applications (CAMA), Nov 2015, pp. 1-3.

[AV20] G. C. Alexandropoulos and E. Vlachos, "A hardware architecture for reconfigu-rable intelligent surfaces with minimal active elements for explicit channel esti-mation," in Proc. IEEE International Conference on Acoustics, Speech, and Signal Processing, Barcelona, Spain, 4-8 May 2020, pp. 9175-9179.

[BG20] J. Budhu and A. Grbic, "Perfectly Reflecting Metasurface Reflectarrays: Mu-tual Coupling Modeling Between Unique Elements Through Homogenization,"

in IEEE Transactions on Antennas and Propagation, vol. 69, no. 1, pp. 122-134, Jan. 2021, doi: 10.1109/TAP.2020.3001450.

[BGM15] L. Bastianelli, L. Giacometti, V. Mariani Primiani, and F. Moglie, "Effect of absorber number and positioning on the power delay profile of a reverberation chamber," in 2015 IEEE International Symposium on Electromagnetic Compatibility (EMC), Dresden, Germany, Aug. 2015, pp. 422-427.

[BKS19J] C. Bucheli et al., "Reconfigurable intelligent surfaces: Bridging the gap between scattering/reflection", arXiv:1912.05344, 2019.

[BLY92] J. H. Beggs, R. J. Luebbers, K. S. Yee, and K. S. Kunz, "Finite-difference time-domain implementation of surface impedance boundary conditions", IEEE Trans. Antennas Propag., vol. 40, no. 1, pp. 49-56, Jan. 1992.

[BMB17] M. Barazzetta, D. Micheli, L. Bastianelli, R. Diamanti, M. Totta, P. Obino, R. Lattanzi, F. Moglie, V. Mariani Primiani, A comparison between different reception diversity schemes of a 4G-LTE base station in reverberation chamber: a deployment in a live cellular network, IEEE Trans. Electromagn. Compat. 59 (6) (2017) 2029-2037. doi:10.1109/TEMC.2017.2657122.

[BMM20] M. Bodehou, E. Martini, S. Maci, I. Huynen, and C. Craeye, "Multibeam and beam scanning with modulated metasur-faces," IEEE Trans. Antennas Propag., vol. 68, no. 3, pp. 1273-1281, Mar. 2020.

[CCR21] D. Chappell, J.J. Crofts, M. Richter, and G. Tanner. "A direction preserving discretization for computing phase-space densities." SIAM Journal on Scientific Computing 43, no. 4, B884-B906, 2021.

[DCD20] L. Di Palma, A. Clemente, L. Dussopt, R. Sauleau, P. Potier, and P. Pouliguen, "Circularly-polarized reconfigurable transmitarray in Ka-band with beam scanning and polarization switching capabilities," IEEE Trans. Antennas Propag., vol. 65, pp. 529-540, Feb. 2017.

[DCS20] F. Diaby, A. Clemente, R. Sauleau, K. Pham, and L. Dussopt, "2-bit reconfigurable unit-cell and electronically steera-ble transmitarray at Ka-band," IEEE Trans. Antennas Propag., accepted for publication, 2020.

[DDT21] M. Di Renzo, F. H. Danufane, S. Tretyakov, "Communication Models for Reconfigurable Intelligent Surfaces: From Surface Electromagnetics to Wireless Networks Optimization," arXiv: 2110.00833, 2021.

[DFV+07] V. Degli-Esposti, F. Fuschini, E. M. Vitucci, G. Falciasecca, “Measure- ment and modelling of scattering from buildings,” IEEE Trans. Antennas Propag., vol. 55 no 1, pp. 143–153, Jan. 2007

[DGL20] C. Della Giovampaola, F. Camminita, G. Labate, E. Martini, and S. Maci, "Reconfigurable metasurface antenna for 5G base stations," in Proc. EuCAP, Copenhagen, Denmark, 2020, pp. 1-6.

[DT21] A. Diaz-Rubio and S. A. Tretyakov, “Macroscopic modeling of anoma- lously reflecting metasurfaces: Angular response and far-field scattering,” IEEE Trans. Antennas Propag., vol. 69, no. 10, pp. 6560–6571, Oct. 2021

[DZD20] M. Di Renzo et al., "Smart Radio Environments Empowered by Reconfigurable Intelligent Surfaces: How It Works, State of Research, and The Road Ahead," in IEEE Journal on Selected Areas in Communications, vol. 38, no. 11, pp. 2450-2525, Nov. 2020, doi: 10.1109/JSAC.2020.3007211.

[FBP21] A. Farasatul, V. Blakaj, S. Phang, T. M. Antonsen, S. C. Creagh, G. Gradoni, and G. Tanner. "Wireless power distributions in multi-cavity systems at high frequencies," Proceedings of the Royal Society A 477, no. 2245, 20200228, 2021.

[FLL04] F. Falcone, T. Lopetegi, M.A.G. Laso, J.D. Baena, J. Bonache, M. Beruete, R. Marqu ?es, F. Mart?n, and M. Sorolla, "Babinet principle applied to the design of metasurfac-es and metamaterials", Phys. Rev. Lett., 93(19):197401, Nov 2004.

[GAA15] G. Gradoni, T. M. Antonsen, S. M. Anlage and E. Ott, "A Statistical Model for the Excitation of Cavities Through Apertures," in IEEE Transactions on Electromagnetic Compatibility, vol. 57, no. 5, pp. 1049-1061, Oct. 2015, doi: 10.1109/TEMC.2015.2421346.

[GD21] G. Gradoni and M. Di Renzo, "End-to-End Mutual Coupling Aware Communication Model for Reconfigurable Intelligent Surfaces: An Electromagnetic-Compliant Approach Based on Mutual Impedances," in IEEE Wireless Communications Letters, vol. 10, no. 5, pp. 938-942, May 2021, doi: 10.1109/LWC.2021.3050826.

[GDA16] J. Gil Gil, Z. B. Drikas, T. D. Andreadis and S. M. Anlage, "Prediction of Induced Voltages on Ports in Complex, Three-Dimensional Enclosures With Apertures, Using the Random Coupling Model," in IEEE Transactions on Electromagnetic Compatibility, vol. 58, no. 5, pp. 1535-1540, Oct. 2016.

[GFE09] Guidelines for evaluation of radio interface technologies for IMT Advanced, International Telecommunication Union - ITU Report M.2135-1, Dec. 2009.

[GTB16] S. B. Glybovski, S. A. Tretyakov, P. A. Belov et al., "Metasurfaces: From microwaves to visible," Phys. Rep., vol. 634, pp. 1 - 72, 2016.

[GYX14] G. Gradoni, J.H. Yeh, B. Xiao, T.M. Antonsen, S.M. Anlage, E. Ott, "Predicting the statistics of wave transport through chaotic cavities by the random coupling model: A review and recent progress.," Wave Motion, 51(4), 606-621, 2014.

[HC09] T. H. Hand and S. A. Cummer, "A dynamic frequency selective surface using ad-dressable metamaterials," 2009 IEEE Ant. and Prop. Soc. Inter. Symp., 2009.

[HC09] T. H. Hand and S. A. Cummer, "A dynamic frequency selective surface using addressable metamaterials," 2009 IEEE Ant. and Prop. Soc. Inter. Symp., 2009.

[HGG16] T. Hartmann, G. Tanner, G. Xie, D. Chappell, J. Bajars. "Modelling of high-frequency structure-borne sound transmission on FEM grids using the Discrete Flow Mapping technique," in Journal of Physics: Conference Series, vol. 744, no. 1, p. 012237. IOP Publishing, 2016.

[HGS08] T.H. Hand, J. Gollub, S. Sajuyigbe, S.A. Cummer, and D.R. Smith, "Characterization of Complementary Electric Field Coupled (CELC) Resonator Surfaces", App. Phys. Lett. 93, 212504, 2008.

[HGS08] T.H. Hand, J. Gollub, S. Sajuyigbe, S.A. Cummer, and D.R. Smith, "Characterization of Complementary Electric Field Coupled (CELC) Resonator Surfaces", App. Phys. Lett. 93, 212504, 2008.

[HSP12] C. L. Holloway, H. A. Shah, R. J. Pirkl, K. A. Remley, D. A. Hill, and J. Ladbury, "Early time behavior in reverberation chambers and its effect on the relationships between coherence bandwidth, chamber decay time, RMS delay spread, and the chamber buildup time," IEEE Trans. Electromagn. Compat., vol. 54, no. 4, pp. 714-725, Aug. 2012.

[HVS17] S. Hubert, A. Vallecchi, A. Schuchinsky and C. Craeye, "Modeling of impedance-loaded sub-wavelength metasurfaces," 2017 International Conference on Electromagnetics in Advanced Applications (ICEAA), 2017, pp. 1041-1044, doi: 10.1109/ICEAA.2017.8065438.

[JRZ21] Z.-M. Jiang, M. Rihan, P. Zhang, L. Huang, Q. Deng, J. Zhang, and E. M. Mohamed, "Intelligent reflecting surface aided dual-function radar and communication system," IEEE Sensors Letters, 2021.

[LPP19] C. Liaskos, G. Pirialakos, A. Pitilakis, S. Abadal, A. Tsioliaridou, A. Tasolamprou, O. Tsilipakos, N. Kantartzis, S. Ioannidis, E. Alarcon, A. Cabellos, M. Kafesaki, A. Pitsillides, K. Kossifos, J. Georgiou, and I. F. Akyildiz, "ABSense: Sensing Electromagnetic Waves on Metasurfaces via Ambient Compilation of Full Absorption," arXiv:1907.04811, July 2019.

[LSR14] C. L”tb„ck Patan,, A. Sk†rbratt, R. Rehammar, C. Orlenius, Basic and advanced MIMO OTA testing of wireless devices using reverberation chamber, in: Proc. 8th Eur. Conf. Antennas Propag., The Hague, Netherlands, 2014, pp. 3488-3492. doi:10.1109/EuCAP.2014.6902581

[LU19] J. S. Lu et al., “A discrete environment-driven GPU-based ray launching algorithm”, IEEE Trans. Antennas Propag., vol. 67 no. 2, pp. 1558–2221,

[MBB20] V. M. Primiani et al., "Reverberation chambers for testing wireless devices and systems," in IEEE Electromagnetic Compatibility Magazine, vol. 9, no. 2, pp. 45-55, 2nd Quarter 2020, doi: 10.1109/MEMC.2020.9133241.

[MBB21] D. Micheli et al., "MIMO 4x4 vs. MIMO 2x2 Performance Assessment of a Real Life LTE Base Station in a Reverberation Chamber", in AEU - International Journal of Electronics and Communications, vol. 129, 2021, https://doi.org/10.1016/j.aeue.2020.153500

[MBC17] D. Micheli, M. Barazzetta, C. Carlini, R. Diamanti, V. Mariani Primiani, F. Moglie, Testing of the carrier aggregation mode for a live LTE base station in reverberation chamber, IEEE Trans. Veh. Technol. 66 (4) (2017) 3024-3033. doi: 10.1109/TVT.2016.2587662.

[MBI17] L. Pulido-Mancera, P. Bowen, M. Imani, N. Kundtz and D. Smith, "Polarizability extraction of complementary metamaterial elements in waveguides for aperture modeling", Phys. Rev. B, vol. 96, no. 23, Nov. 2017.

[MBI17] L. Pulido-Mancera, P. Bowen, M. Imani, N. Kundtz and D. Smith, "Polarizability extraction of complementary metamaterial elements in waveguides for aperture modeling", Phys. Rev. B, vol. 96, no. 23, Nov. 2017.

[MBJ19] Q. Ma, G. D. Bai, H. B. Jing, C. Yang, L. Li, and T. J. Cui, "Smart metasurface with self-adaptively reprogrammable functions," Light Sci Appl, vol. 8, p. 98, Oct. 2019.

[MBM15] D. Micheli, M. Barazzetta, F. Moglie, V. Mariani Primiani, Power boosting and compensation during OTA testing of a real 4G LTE base station in reverberation chamber, IEEE Trans. Electromagn. Compat. 57 (4) (2015) 623-634. doi: 10.1109/TEMC.2015.2434277.

[MBM16] F. Moglie, L. Bastianelli, V. Mariani Primiani, "Reliable Finite-Difference Time-Domain Simulations of Reverberation Chambers by Using Equivalent Volumetric Losses", IEEE Trans. on EMC, vol. 58, no.3, pp. 653-660 June 2016.

[MH73] J. Mautz and R. Harrington, "Modal analysis of loaded N-port scatterers," in IEEE Transactions on Antennas and Propagation, vol. 21, no. 2, pp. 188-199, March 1973, doi: 10.1109/TAP.1973.1140431.

[MPD20] S. Ma, S. Phang, Z. Drikas, B. Addissie, R. Hong, V. Blakaj, G. Gradoni, G. Tanner, T.M. Antonsen, E. Ott, S.M. Anlage, “Efficient statistical model for predicting electromagnetic wave distribution in coupled enclosures,” Physical Review Applied, 8;14(1):014022, Jul 2020.

[NJS21] M. Najafi, V. Jamali, R. Schober and H. V. Poor, "Physics-Based Modeling and Scalable Optimization of Large Intelligent Reflecting Surfaces," in IEEE Transactions on Communications, vol. 69, no. 4, pp. 2673-2691, April 2021, doi: 10.1109/TCOMM.2020.3047098.

[PDP12] Propagation data and prediction methods for the planning of indoor radiocommunication systems and radio local area networks in the frequency range 900 MHz to 100 GHz, International Telecommunication Union - ITU Recommendation P.1238-7, Feb. 2012.

[PDS1] Multipath and Doppler Characterization of an Electromagnetic Environment by Massive MDT Measurements From 3G and 4G Mobile Terminals, https://ieeexplore.ieee.org/document/8620498

[PRL21] Z. Peng, C. Ross, Q. Jian Lim, G. Gradoni, Engineering Reflective Metasurfaces with Ising Hamiltonian and Quantum Annealing, under review, IEEE Transactions on Antennas and Propagation, (https://www.techrxiv.org/articles/preprint/Engineering_Reflective_Metasurfaces_with_Ising_Hamiltonian_and_Quantum_Annealing/14615031/1), 2021.

[PTG18] S. Phang, M. T. Ivrlac, G. Gradoni, S. C. Creagh, G. Tanner and J. A. Nossek, "Near-Field MIMO Communication Links," in IEEE Transactions on Circuits and Systems I: Regular Papers, vol. 65, no. 9, pp. 3027-3036, Sept. 2018, doi: 10.1109/TCSI.2018.2796305.

[PTH20] U. R. Patel, P. Triverio and S. V. Hum, "A Fast Macromodeling Approach to Efficiently Simulate Inhomogeneous Electromagnetic Surfaces," in IEEE Transactions on Antennas and Propagation, vol. 68, no. 11, pp. 7480-7493, Nov. 2020, doi: 10.1109/TAP.2020.3000857.

[QD21] X. Qian and M. D. Renzo, "Mutual Coupling and Unit Cell Aware Optimization for Reconfigurable Intelligent Surfaces," in IEEE Wireless Communications Letters, vol. 10, no. 6, pp. 1183-1187, June 2021, doi: 10.1109/LWC.2021.3061449.

[RVC19] J. R. Reis, M. Vala, R. F. S. Caldeirinha, "Review paper on transmitarray antennas," IEEE Access, vol. 7, pp. 94171-94188, Jun. 2019.

[SGF15] A. Sorrentino, A. Gifuni, G. Ferrara, and M. Migliaccio, "Mode-stirred reverberating chamber autocorrelation function: model, multifrequency measurements and applications," IET Science, Measurement Technology, vol. 9, no. 5, pp. 547-554, 2015.

[SMS06] D. Schurig, J. J. Mock, and D. R. Smith, "Electric-field-coupled resonators for nega-tive permittivity metamaterials", Appl. Phys. Lett. 88, 041109, 2006.

[SMS06] D. Schurig, J. J. Mock, and D. R. Smith, "Electric-field-coupled resonators for negative permittivity metamaterials", Appl. Phys. Lett. 88, 041109, 2006.

[SN17] I. V. Shadrivov and D. N. Neshev, Tunable Metamaterials, World Scientific, 2017, chapter 9, pp. 387-418.

[SPV00] D.R. Smith, W.J. Padilla, D. Vier, S. Nemat-Nasser, and S. Schultz, "Composite medium with simultaneously negative permeability and permittivity", Phys. Rev. Lett., 84(18):4184-4187, May 2000.

[SPV00] D.R. Smith, W.J. Padilla, D. Vier, S. Nemat-Nasser, and S. Schultz, "Composite medium with simultaneously negative permeability and permittivity", Phys. Rev. Lett., 84(18):4184-4187, May 2000.

[SYM17] D. R. Smith, O. Yurduseven, L. P. Mancera, P. Bowen, and N. B. Kundtz, "Analysis of a waveguide fed metasurface antenna," Phys. Rev. App., Nov. 2017.

[SYM17] D. R. Smith, O. Yurduseven, L. P. Mancera, P. Bowen, and N. B. Kundtz, "Analysis of a waveguide fed metasurface antenna," Phys. Rev. App., Nov. 2017.

[TAA21] A. Taha, M. Alrabeiah and A. Alkhateeb, "Enabling Large Intelligent Surfaces With Compressive Sensing and Deep Learning," in IEEE Access, vol. 9, pp. 44304-44321, March 2021.

[TAF95] A. Taflove, "Computational Electrodynamics: The Finite-Difference Time-Domain Method", Norwood, MA: Artech House, 1995.

[TBM14] J. P. Turpin, J. A. Bossard, K. L. Morgan et al., "Reconfigurable and tunable metamaterials: A review of the theory and applications," HINDAWI Int. J. Antennas. Propag., vol. 2014, 429837, 18 pages, 2014.

[V07] O. Roy and M. Vetterli, "The effective rank: A measure of effective dimensionality," 2007 15th European Signal Processing Conference, 2007, pp. 606-610.

[VAC16] Y. Vahabzadeh, K. Achouri and C. Caloz, "Simulation of Metasurfaces in Finite Difference Techniques", in IEEE Transactions on Antennas and Propagation, vol. 64, no. 11, pp. 4753-4759, Nov. 2016, doi: 10.1109/TAP.2016.2601347.

[VCA18] Y. Vahabzadeh, N. Chamanara, K. Achouri and C. Caloz, "Computational Analysis of Metasurfaces", in IEEE Journal on Multiscale and Multiphysics Computational Techniques, vol. 3, pp. 37-49, 2018, doi: 10.1109/JMMCT.2018.2829871.

[VCC18] Y. Vahabzadeh, N. Chamanara, and C. Caloz, "Generalized sheet transition condition FDTD simulation of metasurface", IEEE Trans. Antennas Propag., vol. 66, no. 1, pp. 271-280, Jan. 2018.

[XD21] X. Qian and M. D. Renzo, "Mutual Coupling and Unit Cell Aware Optimization for Reconfigurable Intelligent Surfaces," in IEEE Wireless Communications Letters, vol. 10, no. 6, pp. 1183-1187, June 2021.

[YCY16] H. Yang, X. Caon F. Yang, J. Gao, S. Xu, M. Li, X. Chen, Y. Zhao, Y. Zheng, and S. Li, "A programmable metasur-faces with dynamic polarization, scattering and focusing control," Scientific Reports, 6, 35692, Oct. 2016.

[YFY19] Yang, Fan, and Yahya Rahmat-Samii. Surface Electromagnetics: With Applications in Antenna, Microwave, and Optical Engineering. 2019.

[ZSA21] H. Zhang, N. Shlezinger, I. Alamzadeh, G. C. Alexandropoulos, M. F. Imani, and Y. C. Eldar, "Channel estimation with simultaneous reflecting and sensing reconfigurable intelligent metasurfaces," IEEE International Workshop on Signal Processing Advances in Wireless Communications, Lucca, Italy, 27-30 Sept. 2021.